The Poleward Motion of Extratropical Cyclones from a Potential Vorticity Tendency Analysis

TALIA TAMARIN AND YOHAI KASPI

Department of Earth and Planetary Sciences, Weizmann Institute of Sciences, Rehovot, Israel

(Manuscript received 22 June 2015, in final form 26 October 2015)

ABSTRACT

The poleward propagation of midlatitude storms is studied using a potential vorticity (PV) tendency analysis of cyclone-tracking composites, in an idealized zonally symmetric moist GCM. A detailed PV budget reveals the important role of the upper-level PV and diabatic heating associated with latent heat release. During the growth stage, the classic picture of baroclinic instability emerges, with an upper-level PV to the west of a low-level PV associated with the cyclone. This configuration not only promotes intensification, but also a poleward tendency that results from the nonlinear advection of the low-level anomaly by the upper-level PV. The separate contributions of the upper- and lower-level PV as well as the surface temperature anomaly are analyzed using a piecewise PV inversion, which shows the importance of the upper-level PV anomaly in advecting the cyclone poleward. The PV analysis also emphasizes the crucial role played by latent heat release in the poleward motion of the cyclone. The latent heat release tends to maximize on the northeastern side of cyclones, where the warm and moist air ascends. A positive PV tendency results at lower levels, propagating the anomaly eastward and poleward. It is also shown here that stronger cyclones have stronger latent heat release and poleward advection, hence, larger poleward propagation. Time development of the cyclone composites shows that the poleward propagation increases during the growth stage of the cyclone, as both processes intensify. However, during the decay stage, the vertical alignment of the upper and lower PV anomalies implies that these processes no longer contribute to a poleward tendency.

1. Introduction

The midlatitude atmosphere is dominated by large-scale transient eddies that are an important part of the global circulation; they reduce the equator-to-pole temperature difference by transferring heat and moisture poleward, and are responsible for much of the day-to-day weather variability in the extratropics (e.g., Peixoto and Oort 1992; Vallis 2006). These propagating high and low pressure weather systems have preferred regions of generation, and also follow preferred geographical paths, thus historically named ''storm tracks'' (Chang et al. 2002).

The storm tracks are traditionally defined in either one of the following ways: using an Eulerian approach, as regions of enhanced transient eddy kinetic energy (EKE), obtained using a bandpass time filter with a typical 3–10-day period (e.g., Blackmon et al. 1977); or alternatively, using an ensemble of Lagrangian feature tracking of the storms. The latter identifies the storms, tracks them Lagrangially and then analyzes their statistical distributions (e.g., Hoskins and Hodges 2002). The feature-tracking technique also gives information about what type of systems, cyclones or anticyclones, compose the statistics of the eddy activity and is therefore adopted for the current study.

The two main storm tracks on Earth in the Northern Hemisphere (NH) are localized over the Atlantic and Pacific Oceans. These regions are characterized by strong jets close to the western sides of the ocean basins, and a corresponding downstream maxima in EKE that is tilted poleward (Fig. 1). The poleward deflection has been attributed to local asymmetries such as land–sea contrasts and orography, which give rise to a stationary feature (e.g., Hoskins and Karoly 1981; Held 1983; Held and Ting 1990; Inatsu et al. 2002; Broccoli and Manabe 1992; Brayshaw et al. 2008, 2009; Kaspi and Schneider 2013). The role of transient eddies in these localized storm tracks and their feedback with the mean flow has been the subject of many studies, and is known to have an

Corresponding author address: Talia Tamarin, Department of Earth and Planetary Sciences, Weizmann Institute of Science, 234 Herzl St., Rehovot 7610001, Israel.
E-mail: talia.tamarin@weizmann.ac.il

DOI: 10.1175/JAS-D-15-0168.1

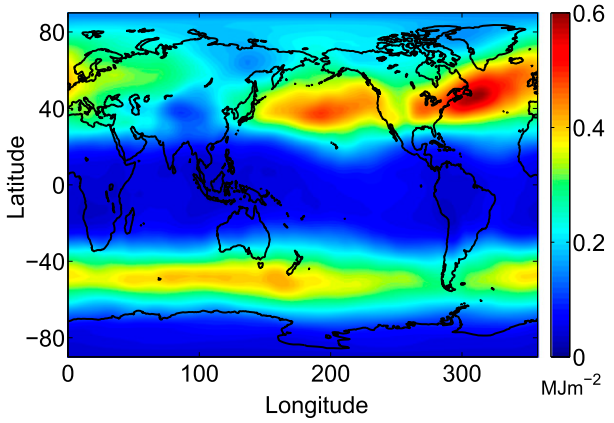

FIG. 1. Vertically integrated EKE (MJ m^{-2}), based on NCEP reanalysis data and calculated using a 3–10-day bandpass filter, averaged over the years 1970–2015 during the NH winter [December–February (DJF)]. NCEP-2 data were provided by the NOAA/OAR/ESRL PSD (http://www.esrl.noaa.gov/psd/).

important influence in shaping the time mean circulation (e.g., Hoskins et al. 1983; Trenberth 1986; Hoskins and Valdes 1990; Orlanski 1998; Cai et al. 2007; Rivière 2009; Novak et al. 2015). Specifically, as was diagnosed in observations by Orlanski (1998), transient eddies play an important role in maintaining the poleward tilt of the localized storm tracks in the NH. In the Southern Hemisphere (SH), a single storm track exists that is more zonally symmetric, due to the lack of longitudinal asymmetries (Trenberth 1991; Nakamura and Shimpo 2004). However, poleward propagation of zonal mean flow anomalies is known to occur in both NH and SH (e.g., Riehl et al. 1950; James et al. 1994; Feldstein 1998; Hoskins and Hodges 2005; Lee et al. 2007; Robinson 2000).

Understanding the tracks of cyclones and anticyclones are of particular interest for the study of climate dynamics, owing to their obvious importance for weather prediction. Observational studies have shown that while cyclones tend to move on average toward the northeast direction, anticyclones exhibit a slight equatorward path and move on average to the southeast (e.g., Petterssen 1956; Macdonald 1967; Klein 1957; Zishka and Smith 1980; Wallace et al.1988; Blender et al. 1997; Mendes and Mendes 2004). It was also shown that cyclones form and intensify in midlatitudes and decay at higher latitudes (Hoskins and Hodges 2005; Sinclair 1997), thus implying poleward propagation. The poleward tendency of cyclones also appeared clearly in studies of specific storms (e.g., Wernli et al. 2002; Rivière et al. 2012), as well as in idealized nonlinear numerical simulations (e.g., Simmons and Hoskins 1978; Davies and Bishop 1994; Schär and Wernli 1993). In addition, it is known that storms often tend to move poleward relative to the jet axis (e.g., Palmen and Newton 1969).

It was recently suggested that the beta-drift mechanism can be generalized to explain the poleward tendency of midlatitude cyclones (Gilet et al. 2009; Oruba et al. 2013; Coronel et al. 2015). In fact, it was already noted by Rossby (1948) that barotropic cyclones (anticyclones) should move poleward (equatorward) due to a ''beta induced'' nonlinear meridional force. The beta drift was mainly discussed in a barotropic context of oceanic vortices (e.g., McWilliams and Flierl 1979), and used to explain the poleward motion of tropical cyclones (e.g., Wu and Emanuel 1993; Holland 1983; Wang and Holland 1996a,b). The poleward motion of midlatitude cyclones was studied by Oruba et al. (2012) and Oruba et al. (2013), who demonstrated the role of upper-level advection in an idealized barotropic and baroclinic quasigeostrophic (QG) two-layer models. Rivière et al. (2012) performed a real case study of a specific storm, and showed how its poleward drift is intensified if the vertically integrated PV gradient is artificially intensified. Recently, Coronel et al. (2015) examined the influence of the upper-level PV and moist processes in the motion of idealized surface cyclones. They performed dry and moist simulations initialized with a low-level PV perturbation and a background zonal jet, with or without an upper-level PV perturbation to its west, and showed how the poleward motion of the low-level PV is enhanced when the upper-level PV and moisture are included.

In this study, we investigate the poleward tendency of cyclones by tracking midlatitude transient eddies in an idealized GCM. The idealized configuration is chosen here for several reasons. First, it allows for long-term statistics to be accumulated. Second, the idealized aquaplanet configuration allows us to simplify the system and rule out processes associated with zonal asymmetries, such as land–sea contrasts. This eliminates stationary waves and demonstrates that the poleward propagation of cyclones can also be achieved without them. The idealized setup, therefore, resembles the SH storm tracks more, since it is zonally symmetric. However, the basic mechanism described here may also explain the poleward tilt of localized storm tracks such as the Pacific and Atlantic NH storm tracks. When zonal asymmetries are present, baroclinicity and associated cyclogenesis are enhanced (e.g., Kaspi and Schneider 2011, 2013), but we speculate that the basic mechanism for poleward propagation is essentially the same. A forthcoming paper will explore idealized GCM experiments that include a localized zonal asymmetry, and will investigate this issue in more detail.

The poleward tendency of cyclones is studied by performing a detailed PV tendency analysis of cyclone composites. The composite allows studying the actual

tendency of the storms throughout their life cycle and tracks, thus to investigate the basic mechanism for poleward propagation. This is as opposed to studying the storm tracks from a statistical perspective, using the time-mean balance at equilibrium, which does not give a complete understanding of how such a balance is achieved.

The advantage of using the PV framework is that it allows us to include and easily interpret the role of diabatic heating (e.g., Davis 1992; Davis et al. 1993; Stoelinga 1996; Lackmann 2002; Posselt and Martin 2004; Ahmadi-Givi et al. 2004). Understanding the influence of latent heat release (LHR) on cyclone dynamics at the individual storm scale has been gaining interest in recent years, due to the expected increase in water vapor content with climate change (Pfahl et al. 2015; Marciano et al. 2015). It is known that diabatic warming often tends to produce a positive PV tendency at lower levels, thus to amplify the PV anomaly associated with the low-level cyclone (e.g., Davis et al. 1993; Ahmadi-Givi et al. 2004). This is especially crucial for type-C cyclogenesis described by Plant et al. (2003), in which the intensification of the surface cyclone is dominated by LHR and can occur even in the absence of a strong temperature gradient. The PV tendency analysis shown here emphasizes the importance of LHR also in propagating the PV anomaly toward the northeast direction.

A straightforward implication of the PV perspective is to employ piecewise PV inversion (Davis and Emanuel 1991; Davis 1992). The piecewise PV inversion allows decomposing the flow field at low levels into its induced velocities from the upper-level PV perturbation, the lower-level PV perturbation, and the surface temperature anomaly. The contribution of each one of them to the advection of the cyclone is studied separately, which reveals the importance of the upper-level PV in advecting the cyclone poleward.

The paper is organized as follows. In section 2 we give a brief description of the idealized GCM and the tracking algorithm. In section 3, tracking results for the propagation of cyclones and anticyclones are presented. In section 4, composite analysis of low-level cyclones is shown, illustrating some of the fundamental characteristics of cyclones that are relevant for the poleward motion. Section 5 presents the contribution of the horizontal advection terms to the PV tendency, and piecewise PV inversion is performed and discussed. Section 6 concentrates on the PV tendency from the diabatic terms. The mechanisms responsible for the poleward propagation are discussed in each case. In addition, we present the time development of the cyclone composites in section 7, and how it varies with intensity in section 8. The summary and conclusions are given in section 9.

2. Numerical methods

a. Idealized GCM

The idealized GCM is based on the GFDL Flexible Modeling System (FMS), which solves the three-dimensional primitive equations of an ideal-gas atmosphere in spherical coordinates. The equations are solved using a standard spectral dynamical core and a finite-difference time integration. We use a resolution with spectral triangular truncation of T85, which corresponds to a horizontal grid resolution of $1.4° \times 1.4°$, and 30 vertical sigma levels. The model includes a simplified representation for water vapor and a simplified radiation scheme (Frierson et al. 2006). The model has no continents or topography, it is an aquaplanet (ocean covered) Earth in which the lower boundary is a uniform slab ocean with a specified heat capacity and an energy-conserving balance. The boundary layer surface temperatures are not prescribed in this model, but rather are a response to changes in surface fluxes of radiative energy, latent heat, and sensible heat. Radiation is represented by a standard two-stream radiation scheme, in which longwave and shortwave optical depths depend only on latitude and pressure (Held 1982). In this idealized simulation, we use a top-of-the-atmosphere solar insolation of perpetual equinox. Moist convection relaxes temperature profiles toward a moist adiabat, and a large-scale condensation scheme removes condensed water vapor from the atmosphere when the specific humidity exceeds saturation in a grid point (Frierson et al. 2006). Hence, water vapor is only removed from the atmosphere by precipitation. The idealized model does not include clouds, continents, ice, and chemical processes. However, it still obtains to leading order a similar climate to that observed on Earth. The model is first run for a spinup time of 2000 days until it reaches statistical equilibrium, and only then the fields are used for further analysis.

b. Storm-tracking algorithm

In this study, we use a feature-point tracking technique to study extratropical cyclones, which is often used to produce spatial diagnostics for their statistics (e.g., Sinclair 1994; Hodges 1995; Hodges et al. 2003; Hoskins and Hodges 2002, 2005). The tracking algorithm used here is that developed by Hodges (1995) and Hodges (1999), which performs the tracking on the unit sphere. The storms are identified by a maximum or minimum in the pressure field, and followed using the model output every 6 h. To avoid noise, the fields are first reduced to a T42 Gaussian grid, and the spectral coefficients have a tapering filter applied to reduce any Gibbs noise (Sardeshmukh and Hoskins 1984). The

tracks are found using a nearest-neighbor approach and minimizing a cost function for the ensemble track smoothness. The background field (spatial wavenumber smaller than five) is removed before the tracking, in order to isolate the synoptic spatial scale variability. Only mobile storms that last for more than 2 days and move more than 1000 km are kept for the analysis. The tracking results are then used to construct composites of all midlatitude cyclones, as will be explained in detail in section 4, which are used to perform the PV tendency analysis presented in sections 4–8.

3. Tracking results

We perform the tracking on an aquaplanet configuration of the GCM with no zonal asymmetries, accumulating separate statistics for cyclones and anticyclones. The dynamics studied here, therefore, resemble better those of the SH on Earth, which are characterized by a more zonally symmetric storm track compared to the localized storm tracks in the NH (Fig. 1). A snapshot from the simulation is shown in Fig. 2, with pressure zonal anomalies at 780 hPa (colors) and geopotential height at 300 hPa (black contours). Also plotted are the low-level pressure centers (white dots), identified by the tracking algorithm. It is evident that the tracking works well in capturing the low-level pressure centers of the main features. The algorithm then follows the center of each pressure anomaly, and statistics for their tracks are collected for further analysis.

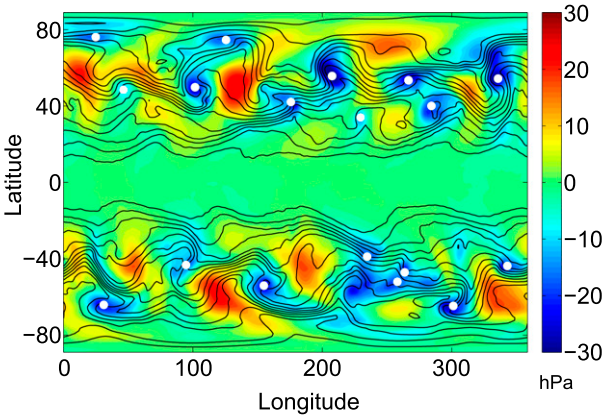

FIG. 2. A snapshot from the simulation. Shown are geopotential height at 300 hPa (black contours) and pressure zonal anomalies at 780 hPa (color bar; hPa). White dots are the low pressure centers as identified by the tracking algorithm.

The actual tracks of approximately 1000 pressure systems at 780 hPa, which first appeared between latitudes 20° and 60° in the NH, are shown for cyclones and anticyclones (Figs. 3a and 3c, respectively), where colors indicate the intensity of the systems (in units of hPa). The level of 780 hPa is chosen here as representing the average of the lower layers. In Figs. 3b,d all the tracks are translated to start from the origin, and the black

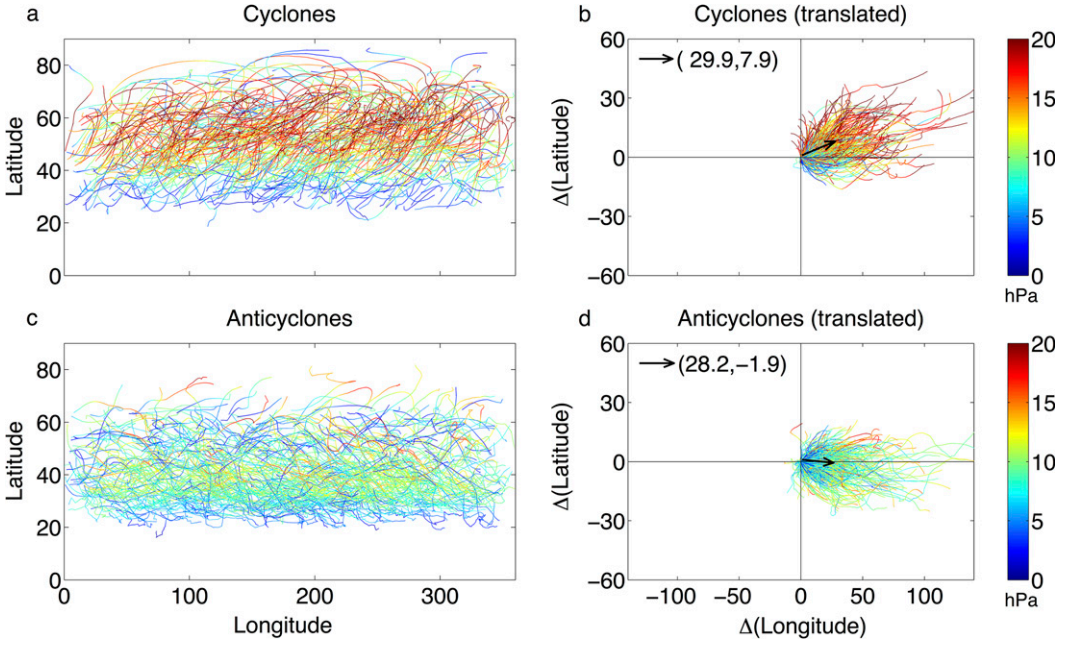

FIG. 3. Tracks for lower-level (780 hPa) (a),(b) cyclones and (c),(d) anticyclones, with color indicating the intensity of the system (hPa). In (b),(d), the tracks are translated to a common starting point and black arrows show the averaged track.

arrow points toward the averaged final position. Although these simulations are zonally symmetric, there is a latitudinal drift during the path of each storm. The benefit of plotting the actual tracks instead of the time mean or zonally averaged track density is that the poleward propagation can be clearly seen. Low-level cyclones tend to propagate mainly poleward, whereas anticyclones exhibit both equatorward and poleward tracks. There is an indication that cyclones intensify as they travel poleward, and that stronger cyclones also propagate more poleward. Anticyclones, which are generally much weaker than cyclones, also seem to intensify as they travel, but do not exhibit a clear latitudinal bias for stronger intensities.

The averaged track (black arrow in Figs. 3b,d) shows that the average cyclone drifts 7.9° in latitude poleward and 29.9° in longitude eastward, while the averaged anticyclone has a small equatorward drift of −1.9° in latitude and 28.2° in longitude eastward. For cyclones at midlatitudes, this corresponds roughly to a deflection of 1300 km poleward, as they travel 3500 km eastward (assuming an averaged latitude of 45°). Note that these averages take into account all storms identified at midlatitudes, regardless of their size, intensity, or any other dynamical difference between them. Hence, there is a large spread in the tracks shown in Figs. 3b,d. Nonetheless, the cyclones in our simulation clearly tend to propagate more poleward than anticyclones. This is in agreement with observational studies (e.g., Macdonald 1967; Storari and MacDonald 1973; Blender et al. 1997), who found a similar poleward deflection of cyclones. In the following sections, we explore this fundamental poleward tendency of cyclones by performing a composite analysis of midlatitude cyclones, and analyzing their dynamics from a PV perspective.

4. Cyclone composites and PV tendency analysis

a. Cyclone-tracking composites

The tracking data are used to construct composites of cyclones. For each cyclone, a box sized 30° in latitude by 40° in longitude is placed around its center (i.e., around each white dot in Fig. 2), at every time step. Each cyclone is tracked during its growth stage, until it reaches maximum intensity. Fields of interest are being accumulated along the trajectory, and then averaged together with all other tracks. The composites presented in this section are averaged over approximately 1000 storms, taking snapshots every 6 h along the trajectory of each storm.

The composite analysis in the idealized GCM configuration used here is consistent with cyclone composites of reanalysis data and full GCMs (e.g., Catto et al. 2010; Bauer and Del Genio 2006). The main features of extratropical cyclones, such as temperature fronts and the warm conveyer belt, can be identified in the composites (Fig. 4). Looking at the position of the low-level cyclone shows the classic picture of baroclinic instability (e.g., Martin 2006), where the low-level cyclone is located on the eastward side of an upper-level open-wave trough (Fig. 4a). This has an important implication for the poleward propagation, as will be shown in the next section. In the quasigeostrophic framework, the upper-level divergence on the eastward side of the trough, explained using either the omega equation or the ageostophic divergence (e.g., Martin 2006), is accompanied by rising air (Fig. 4b) and surface convergence, associated with the low pressure anomaly. The eastern side of the cyclone is also characterized by strong poleward meridional wind (Fig. 4c) that lies in a region of high equivalent potential temperature θ_E (Fig. 4d). This is associated with the warm conveyer belt (Harrold 1973), which acts to bring moist and warm subtropical air poleward and upward. This results in LHR, which in turn influences the cyclogenesis process. As will be shown, the LHR is also important for the cyclone's poleward motion.

b. PV tendency analysis

From a PV perspective, which is taken here, cyclogenesis can be described as the mutual interaction between an upper-level PV anomaly and a lower-level one to its east (Bretherton 1966). The advantage of using a PV approach is the relatively simple way of including the influence of diabatic heating on the dynamics. In the following sections we will analyze the different contributions to the PV tendency equation, and show the crucial role of moisture and the upper-level PV in the poleward motion of the cyclone.

The Ertel PV in pressure coordinates, defined as

$$q = -g(f\mathbf{k} + \nabla_p \times \mathbf{u}) \cdot \nabla_p \theta, \tag{1}$$

satisfies the equation

$$\frac{dq}{dt} = Q + F, \tag{2}$$

where $\nabla_p = (\partial/\partial x, \partial/\partial y, \partial/\partial p)$ is the gradient operator in pressure coordinates, $d/dt = \partial/\partial t + u\partial/\partial x + v\partial/\partial y + \omega\partial/\partial p$ is the material derivative with $\omega = dp/dt$, g is the gravitational acceleration, f is the planetary vorticity, $\nabla_p \times \mathbf{u}$ is the relative vorticity, and θ is the potential temperature. Note that the horizontal derivatives are calculated on a sphere (i.e., $\partial/\partial x = \partial/R\cos\theta\partial\phi$ and $\partial/\partial y = \partial/R\partial\theta$, where ϕ and θ are the zonal and meridional coordinates, respectively, and R is the radius of Earth). The

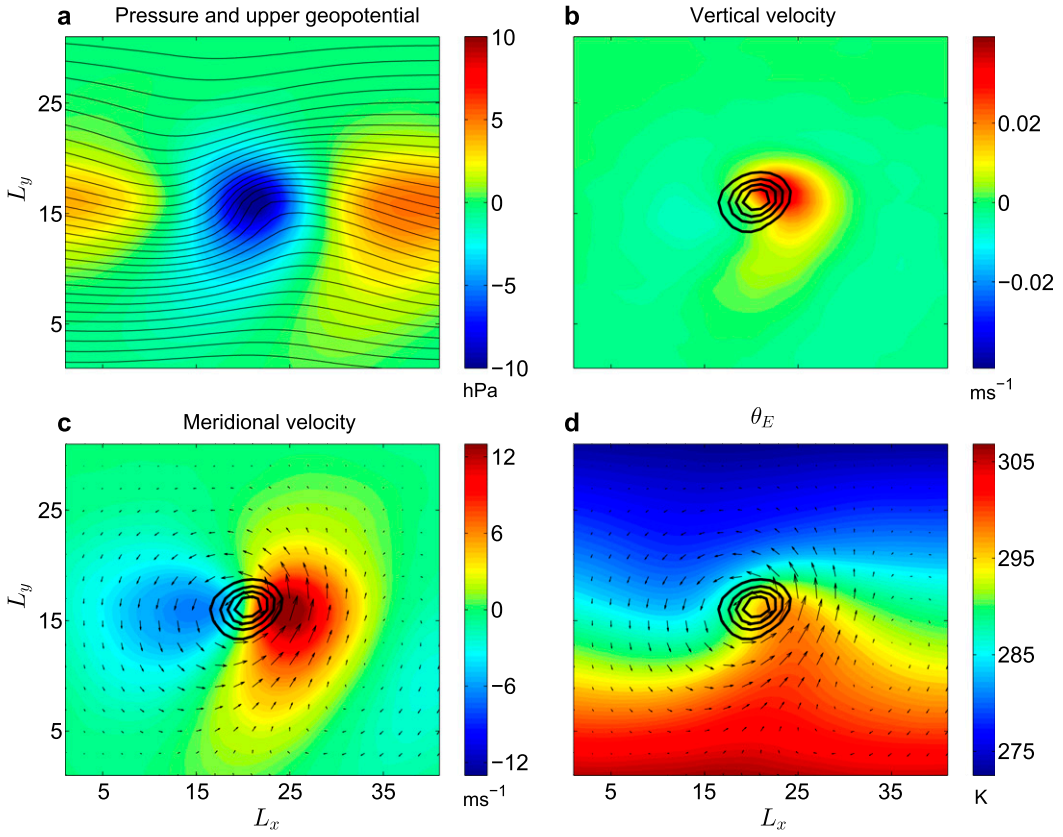

FIG. 4. Cyclone composites at lower levels (780 hPa) of (a) pressure anomaly (hPa), (b) vertical velocity (m s^{-1}), (c) meridional velocity (m s^{-1}), and (d) equivalent potential temperature (K). In (a), the black contours show the upper-level (300 hPa) geopotential height. In (c),(d), the black arrows are the perturbation horizontal winds from the composite at 780 hPa. The black contours in (b)–(d) show the 780-hPa PV anomaly, with contours from 0.15 to 0.42 PVU and contour interval of 0.09 PVU. The longitudinal and latitudinal extents of the composite box are denoted by L_x and L_y, respectively.

rhs includes nonconservative processes such as diabatic heating, given by

$$Q = -g(f\mathbf{k} + \nabla_p \times \mathbf{u}) \cdot \nabla_p \left(\frac{d\theta}{dt}\right) \tag{3}$$

and a friction term F. In the absence of friction ($F = 0$), adiabatic motion ($Q = 0$) will conserve its PV, which is why PV is considered an insightful conceptual approach. At the 780-hPa level considered here, the friction term can be neglected to leading order. The main contributors to the PV tendency are thus the horizontal advection terms, the vertical advection, and the diabatic terms, which include LHR and radiation (internal dissipation has negligible contribution and is therefore neglected).

The tracks of low-level cyclones are used to construct a composite of the Ertel PV budget (note that the results are almost identical if vorticity features are tracked instead). The lower-level PV (780 hPa) anomaly (black contour in Fig. 5) is located in the middle of the box, implying that lower pressures are associated with positive PV anomalies. The upper-level PV field (colored contours) is deformed by the low-level cyclonic winds (not shown). There is a signature of the deepening process of the upper-level PV, which leads eventually to the treble clef shape characteristic of a mature occluded cyclone (Posselt and Martin 2004). The location of the low-level PV anomaly to the east of the positive upper PV maximum implies that the upper-level winds (black arrows in Fig. 5) induce positive meridional velocities on the low-level cyclone. This configuration is not only favorable for the cyclone's growth, but also contributes to its poleward motion. The total PV tendency at lower levels (red contours are positive values and blue are negative in Fig. 5) reveals that PV destruction occurs at the southwestern side of the low-level cyclone, while positive PV tendency occurs on its northeastern side. Hence, the total motion of the cyclone and its associated positive PV anomaly is eastward and poleward.

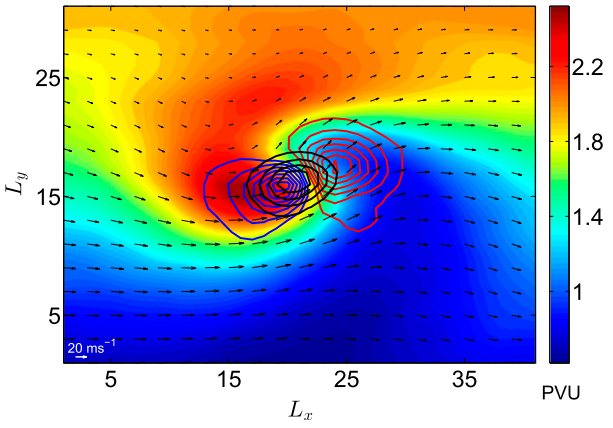

FIG. 5. Cyclone composites of the PV anomaly at lower levels (780 hPa; black contours) and PV at upper levels (300 hPa; colored), superimposed with total PV tendency at lower levels (red contours are positive values and blue contours negative values). Low-level PV contours range from 0.15 to 0.42 PVU (with contour interval of 0.09 PVU). The PV tendency contour values range from 1.5×10^{-6} to 8.4×10^{-6} PVU s^{-1} for the positive values (with contour interval of 1.15×10^{-6} PVU s^{-1}), and from -9.5×10^{-6} to -1.5×10^{-6} PVU s^{-1} for the negative values (with contour interval of 1.3×10^{-6} PVU s^{-1}). The black arrows show the composite of upper-level winds, with a reference wind vector (white arrow in the bottom left) included to indicate the wind strength at upper levels. The longitudinal and latitudinal extents of the composite box are denoted by L_x and L_y, respectively.

A quantitative analysis of the separate contributions to the PV tendency at lower levels is performed next. We first decompose the flow into a background flow and a perturbation. The background flow is chosen to be the climatological mean. This choice is particularly convenient since it is both time independent and zonally symmetric (as long as statistics are accumulated for long enough), that is, in our decomposition, $a(x, y, p, t) = \overline{a(y, p)} + a'(x, y, p, t)$, where a is any field of interest.

Since the meridional background flow $\overline{v}$ is small, its contributions to the tendency equation are an order of magnitude smaller. It follows that the PV tendency equation for our analysis can be approximately written as

$$\frac{\partial q'}{\partial t} = -\overline{u}\frac{\partial q'}{\partial x} - v'\frac{\partial \overline{q}}{\partial y} - u'\frac{\partial q'}{\partial x} - v'\frac{\partial q'}{\partial y} - \omega\frac{\partial q}{\partial p} + Q. \qquad (4)$$

The first term on the rhs denotes the advection of the PV perturbation by the background zonal mean flow. The second term is the meridional advection of the background vorticity by the perturbation velocity associated with the cyclone, which in the PV perspective is the term related to the Rossby wave propagation. The next two terms are the nonlinear perturbation advection terms, and the last two terms are the vertical advection and diabatic heating Q, respectively. The contribution of the advection terms and the diabatic terms to the PV tendency equation are analyzed next in the following two sections.

5. Horizontal advection terms and piecewise PV inversion

a. PV tendency from horizontal advection terms

The horizontal advection terms from Eq. (4) for the low-level PV are calculated separately and plotted in Fig. 6. In Figs. 6a–f, the low-level PV anomaly (defined here as the PV at 780 hPa relative to the climatological composite at that level), is shown in black contours for reference. The zonal advection of the low-level PV by the background flow (Fig. 6a) gives the expected eastward advection of the anomaly, hence, positive (negative) PV tendency to the east (west). The black arrows show the background zonal flow, which is eastward and slightly decreases poleward, implying that the average cyclone resides on the poleward flank of the jet. The advection of the mean PV by the perturbation meridional wind (Fig. 6b) tends to propagate the anomaly westward. The low-level perturbation horizontal winds are also shown (black arrows). This term is the classic Rossby wave propagation mechanism (Rossby 1948); since the background PV increases poleward,[1] a positive PV anomaly, which is associated with cyclonic winds, advects high (low) PV to its west (east). This produces a positive (negative) anomaly to its west (east), so the perturbation propagates westward. Note that the contribution of this term is weaker than the opposite contribution of the zonal advection of the perturbation PV (Fig. 6a), consistent with the overall eastward motion of the low-level PV anomaly.

The nonlinear terms tend to propagate the anomaly poleward and slightly westward (Fig. 6c). Decomposing the nonlinear advection into contributions from the zonal and meridional directions (Figs. 6d and 6e, respectively) shows that each of them is characterized by a quadrupole structure. However, the meridional advection term is characterized by much weaker magnitudes on the western side. This is a result of the stronger magnitude of poleward velocity on the eastern side of the cyclone relative to the western side (Fig. 4c).

In fact, the horizontal nonlinear advection terms of an idealized symmetric cyclone should cancel out exactly,

[1] The background flow, defined as the zonal mean of the climatology composite, reflects mostly the beta term and, hence, increases toward the pole.

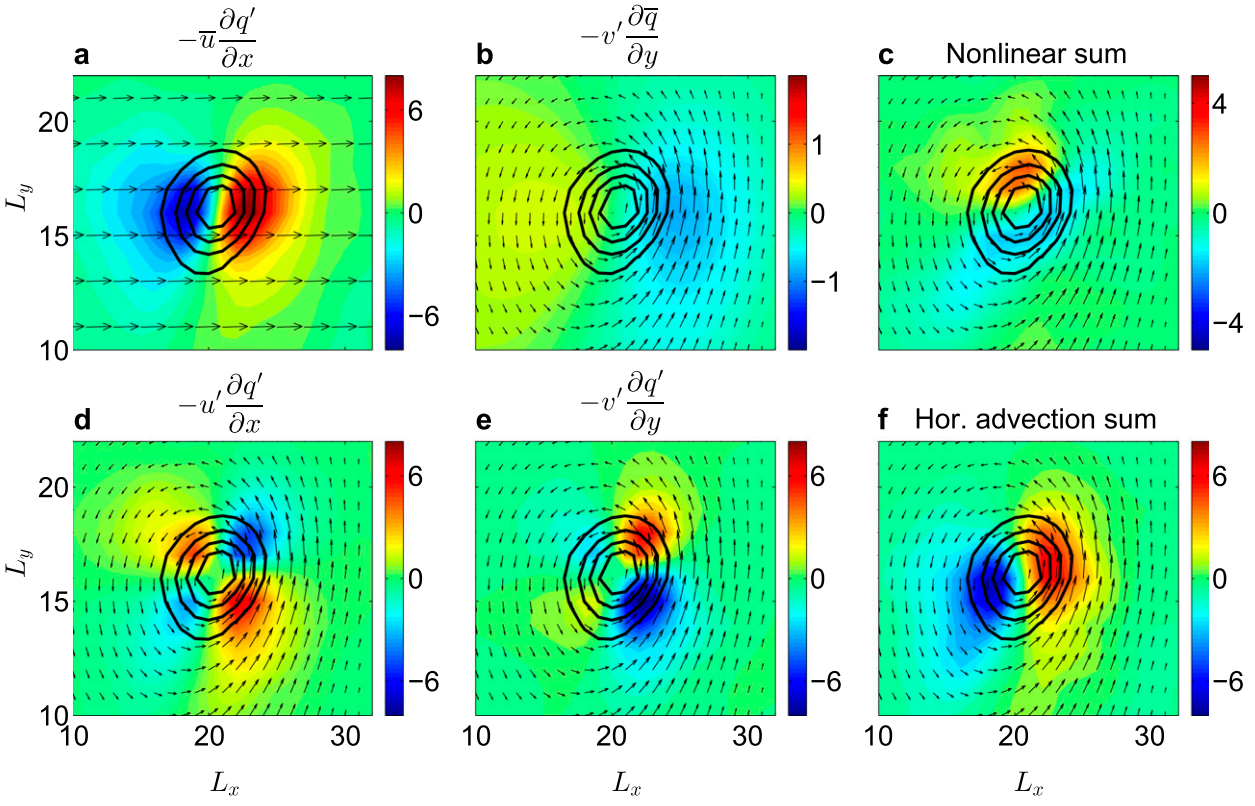

FIG. 6. The low-level (780 hPa) PV tendency from (a) advection of PV perturbation by the background zonal velocity, (b) advection of background PV by the meridional perturbation velocity, (c) sum of nonlinear advection terms, (d) nonlinear zonal advection, (e) nonlinear meridional advection, and (f) total sum of horizontal advection terms. All quantities are normalized by 10^{-6} PVU s^{-1}. The black arrows in (f) show the total low-level winds, in (d) the mean low-level winds are shown, and in all other panels the perturbation low-level winds are shown. The black contours in all panels show the 780-hPa PV anomaly, with contours from 0.15 to 0.42 PVU and contour interval of 0.09 PVU. The longitudinal and latitudinal extents of the composite box are denoted by L_x and L_y, respectively.

in analogy to a point vortex that cannot move itself. This is illustrated schematically in Fig. 7. The zonal and meridional nonlinear PV advection terms of a symmetric cyclone (Figs. 7a and 7b, respectively), each create a symmetric quadrupole structure of PV tendency, but of opposite sign. Since PV decreases from the center of the PV anomaly, positive meridional velocity on the eastern side of the cyclones advects high PV to the northeastern corner of the PV, producing a positive PV anomaly, and low PV to the southeastern side of the PV anomaly, producing a negative PV anomaly there. The opposite occurs on the western side of the cyclone, where the meridional cyclonic wind is negative. The same argument explains why the nonlinear advection term in the zonal direction acts to produces negative PV anomaly on the northeastern and southwestern corners, and a positive PV tendency on the northwestern and southeastern corners. Hence, the overall horizontal advection terms of a symmetric cyclone cancel each other exactly, and, therefore, do not contribute to any net propagation of the cyclone.

The zonal and meridional nonlinear advection terms clearly do not cancel out in the cyclone composites (Fig. 6c). Thus, the nonlinear terms produce a poleward and slightly westward tendency, which is significant for the poleward motion of the low-level cyclone. The total sum of the horizontal advection terms (Fig. 6f) is characterized by a positive PV tendency in the northeastern side of the low-level PV anomaly, and a negative PV tendency on the southwestern side of the low-level PV anomaly. This gives an overall eastward and poleward advection of the low-level PV.

The apparent strong asymmetry between the zonal and meridional nonlinear advection terms, which is crucial for creating the poleward tendency, provides a hint for the role of the upper-level anomaly in advecting the cyclone poleward. To study the origin of this asymmetry, we next decompose the low-level velocity using the piecewise PV inversion technique developed by Davis and Emanuel (1991) and Davis (1992). This allows decomposing the nonlinear PV

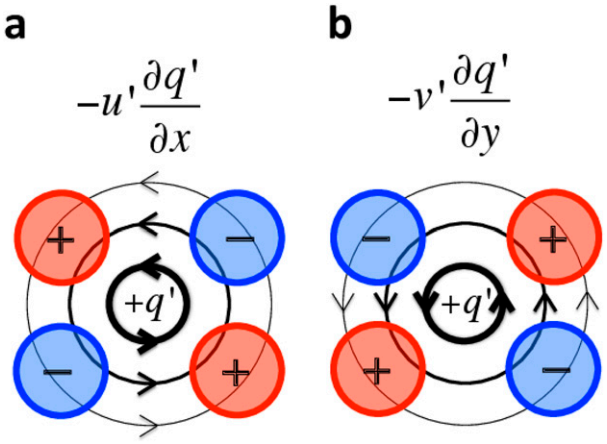

FIG. 7. A schematic illustration of the PV tendency from the "self induced" nonlinear terms of a positive axisymmetric PV anomaly. The nonlinear PV advection in the (a) zonal and (b) meridional directions form two antisymmetric quadrupoles, hence, the overall nonlinear tendency from the self-advection of an idealized PV anomaly is canceled out.

advection term into a contribution originating from the upper-level PV, the lower-level PV, and the surface temperature anomaly, and to distinguish what is the influence of each of them in isolation. We demonstrate the important role played by the upper-level PV in this asymmetry, which results in a strong positive meridional velocity that contributes to the poleward tendency of the cyclone. The details of the algorithm, decomposition, and composite analysis of the piecewise PV inversion are presented next.

b. *Composites of piecewise PV inversion*

To quantify the contribution from the upper-level PV to the PV tendency of the lower PV, we perform a piecewise PV inversion (Davis and Emanuel 1991). The invertability of PV is one of its basic and most powerful characteristics (Hoskins et al. 1985). Given a distribution of PV, one can invert back the field and find the balanced wind, pressure, and temperature associated with that PV field. Piecewise inversion (Davis 1992) allows one to decompose the flow into several significant parts (e.g., different vertical levels), and the PV associated with each one of them can be studied separately. Previous studies used piecewise PV inversion to study the role of upper and lower PV anomalies in the extratropical cyclogenesis process (e.g., Davis and Emanuel 1991; Davis 1992; Black and Dole 1993; Hakim et al. 1996; Huo et al. 1999a,b; Brennan et al. 2008; Rosting and Kristjansson 2012), the role of moisture and LHR in the storm development (e.g., Stoelinga 1996; Lackmann 2002; Posselt and Martin 2004; Ahmadi-Givi et al. 2004), and to the study tropical cyclones and hurricanes (e.g., Wu and Emanuel 1995; Wang and Zhang 2003; Kieu and Zhang 2010).

The piecewise PV inversion algorithm of Davis and Emanuel (1991) is used here, which employs the nonlinear balance equation of Charney (1955). This is similar to the gradient wind balance, and thus gives good results for highly curved flows. The linearized version of the Charney balance is essentially the quasigeostrophic balance equation. The balanced equations are solved using a standard successive overrelaxation technique (for full details see Davis and Emanuel 1991; Davis 1992). Each piecewise inversion is achieved by setting the other PV perturbations to zero, and using homogeneous lateral boundary conditions. The piecewise inversion procedure returns the balanced three-dimensional streamfunction and geopotential height associated with each of the anomalies considered. Thus, winds originating from specific PV perturbations can be derived at any level of interest.

We follow Davis and Emanuel (1991) and decompose the flow field into three components: the upper-level Ertel PV perturbation (780 hPa and above, denoted UPV), the lower-level Ertel PV perturbation (780 hPa and below, denoted LPV), and the surface temperature anomaly (potential temperature at 980 hPa, denoted as θ_S). This idealization of the flow is based on Hoskins et al. (1985), who describe baroclinic instability as the interaction and mutual amplification of two counterpropagating Rossby waves, similar to the classic models of Eady (1949) and Charney (1947) and described also by Bretherton (1966).

A composite analysis of the piecewise inversions is done in the following manner. For each cyclone identified we perform a piecewise PV inversion in a box around its center, for each time step. The inversion is employed every 6 h during the time development of the cyclone, until it reaches maximum intensity, and then averaged for each cyclone. The composite of piecewise PV inversions is then calculated as the mean over all cyclones identified.

To study the different contributions to the low-level meridional PV tendency term, we decompose the 780-hPa wind into velocities induced from upper-level PV (black arrows in Fig. 8a), lower-level PV (black arrows in Fig. 8b), and from the surface temperature anomaly (black arrows in Fig. 8c). The wind induced from θ_S (Fig. 8c) is almost opposite to that induced by the upper-level PV, since the temperature anomaly is approximately one-half wavelength out of phase with the UPV.

The different contributions of each PV perturbation to the zonal and meridional nonlinear PV tendency advection terms (the original terms in Figs. 6d and 6e, which should be compared with the recovered ones in

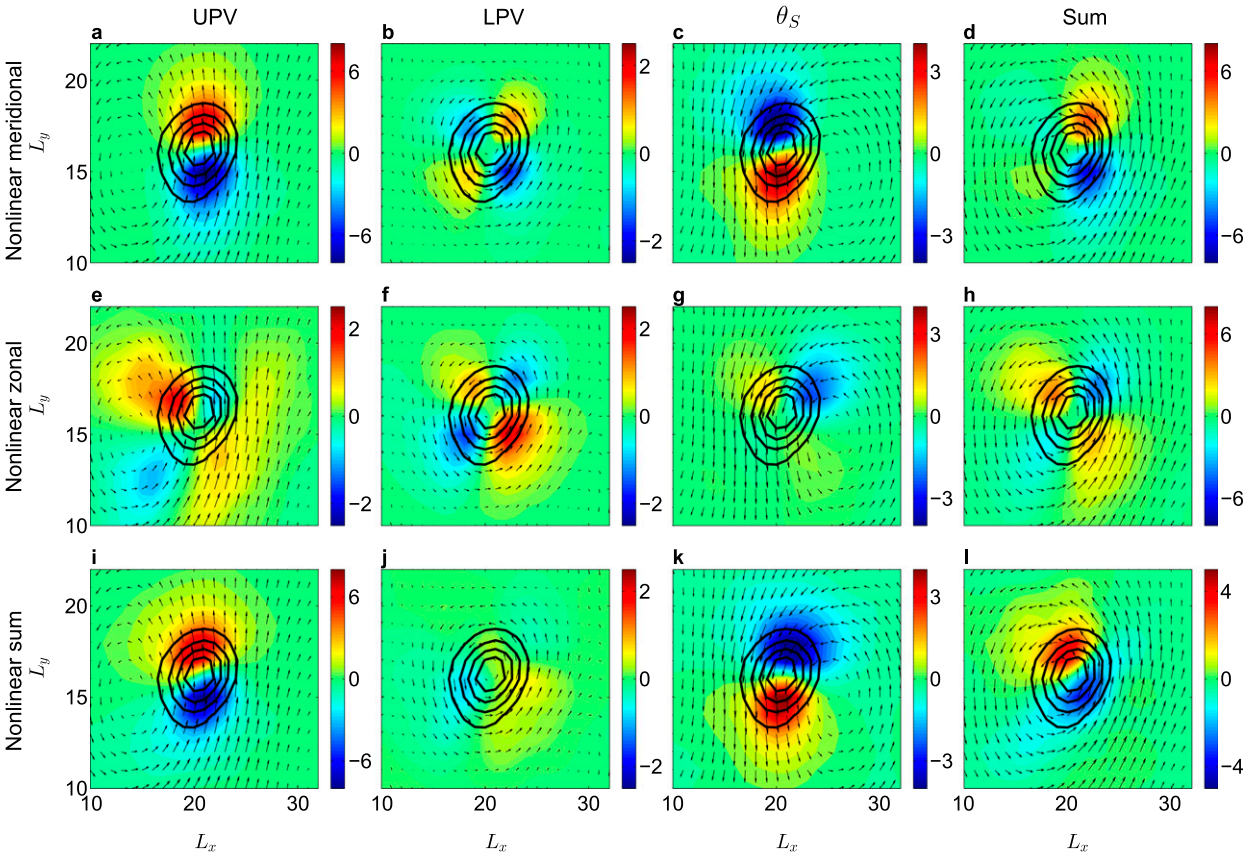

FIG. 8. Piecewise PV decomposition of the nonlinear PV advection terms. Contribution to the PV tendency at 780 hPa from (a)–(d) the meridional nonlinear advection, (e)–(h) the zonal nonlinear advection, and (i)–(l) the sum of the nonlinear advection terms. (left)–(right) The contributions to the PV tendency at 780 hPa from the UPV, the LPV, the θ_S anomaly, and the sum. All quantities are normalized by 10^{-6} PVU s^{-1}. In each panel the associated winds (black arrows) induced by each of the PV pieces (UPV, LPV, θ_S, and the total PV) are added. The PV anomaly at 780 hPa is also shown in all panels for reference, with contours from 0.15 to 0.42 PVU and contour interval of 0.09 PVU. The longitudinal and latitudinal extents of the composite box are denoted by L_x and L_y, respectively.

Figs. 8d and 8h, respectively) are shown in Fig. 8. The meridional nonlinear advection from the UPV (Fig. 8a) produces a positive and negative PV tendency on the northern and southern sides of the low-level PV anomaly, respectively, and thus advects the low-level cyclone poleward. This is consistent with the positive meridional velocity it induces at lower levels (black arrows). The zonal nonlinear PV advection from the UPV (Fig. 8e) is maximized on the northwestern side of the low-level PV, although it is much weaker than the meridional nonlinear term. This reflects the weak-induced zonal velocities from upper levels, compared to meridional velocities. Their sum (Fig. 8i) is indeed entirely dominated by the meridional nonlinear PV advection.

The velocity field induced by the UPV is in fact characterized by two gyres that are a baroclinic version of the barotropic "beta gyres" (induced by the UPV perturbation rather the lower PV anomaly itself). These results are consistent with Gilet et al. (2009) and Oruba et al. (2013), who showed in idealized two-layer quasi-geostrophic experiments how the upper-level PV advects the low-level PV when the two are initialized such that the upper-level PV is to the west of the low-level PV. The westward tilt with height, which is a characteristic of baroclinic instability, implies that the upper-level PV induces poleward meridional velocity on the low-level PV associated with the cyclone.

In contrast, the meridional nonlinear PV advection associated with the θ_S anomaly tends to advect the low-level cyclone equatorward (Fig. 8c). Since the low-level PV anomaly is slightly to the west of the PV anomaly associated with θ_S, but to the east of the UPV, it is influenced by them in opposite directions. This is illustrated in the schematic Fig. 9, which is based on the classic conceptual picture of interacting PV anomalies as in Hoskins et al. (1985). The zonal nonlinear PV advection associated with the surface potential temperature (Fig. 8g) is weaker, and mainly

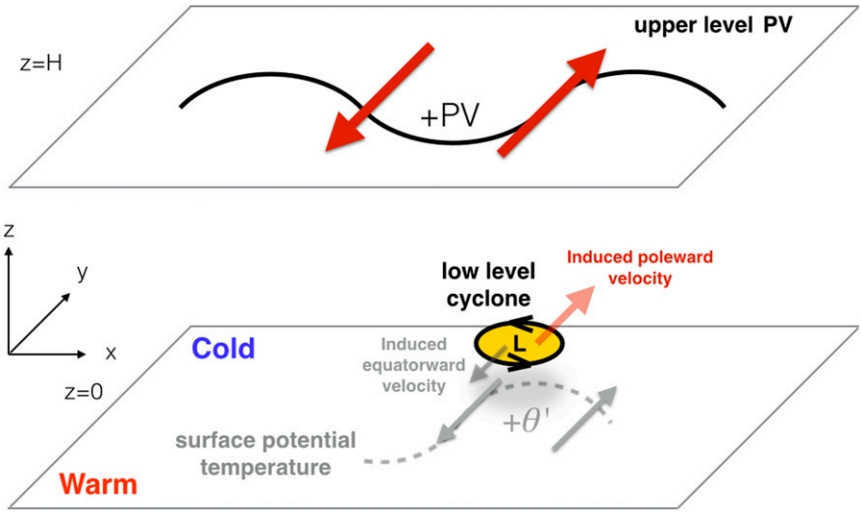

FIG. 9. A schematic diagram illustrating the influence of upper-level PV and surface potential temperature anomaly on the lower-level PV associated with the low-level cyclone. The two layers represent the surface ($z = 0$) and the tropopause ($z = H$). The solid line at the upper layer represent the upper-level PV wave, the plus sign marks positive PV, and solid brown arrows are the velocities associated with the positive PV anomaly at upper levels. The dashed gray line at the lower level represents an isotropic line, and gray arrows represent the circulation associated with that PV anomaly. The yellow circle with "L" in the middle is the low-level (780 hPa) cyclone, and the light arrows show the induced poleward velocity from the upper-level PV (light red) and from the surface potential temperature anomaly (light gray).

advects westward the northern side of the low-level PV. The sum of the nonlinear advection terms associated with the surface potential temperature (Fig. 8k) is again dominated by the meridional nonlinear advection.

The meridional and zonal nonlinear PV advection terms from the winds induced by the LPV, associated with the low-level cyclone itself, (Figs. 8b and 8f, respectively), show a more symmetric quadrupole structure that is similar and opposite in sign, as expected. This structure is a result of the self-advection of the cyclone in the zonal and meridional directions, just like in the schematic in Fig. 7. The sum of the meridional and zonal nonlinear PV advection terms induced by the LPV (Fig. 8j) is indeed small. Hence, these terms do not contribute significantly to the propagation of the low-level cyclone. Note that the cancelation is not complete, probably because the low-level PV is not perfectly axisymmetric.

The sum of the PV tendency from the meridional and zonal nonlinear advection terms at lower levels (Fig. 8d that is the sum of Figs. 8a–c, and Fig. 8h that is the sum of Figs. 8e–g), are similar to the original terms (Figs. 6e and 6d, respectively). Accordingly, the total sum of the horizontal nonlinear PV advection terms at lower levels (Fig. 8l that is the sum of Figs. 8d,h or alternatively Figs. 8i–k) is similar to the original term (Fig. 6c). This proves that the inversion procedure recovers well the wind field.

The overall sum (Fig. 8l) gives, as before, a poleward and slightly westward advection of the low-level PV. Combined with the eastward zonal advection by the mean background flow, this gives an eastward and poleward advection of the low-level PV (similar to Fig. 6f), which is consistent with the observed motion of the low-level cyclones. The decomposition of the nonlinear advection term presented here shows clearly the important role of the meridional advection by the UPV in the poleward tendency of the low-level PV anomaly.

6. Diabatic heating and vertical advection

Next, we present the contributions of the diabatic heating terms to the PV tendency [Eq. (3)], arising from LHR (Fig. 10a) and the background radiation (Fig. 10b). Diabatic processes associated with extratropical cyclones have been studied extensively, and are known to have an important role in the cyclogenesis process (e.g., Reed et al. 1992; Davis et al. 1993; Stoelinga 1996; Posselt and Martin 2004; Ahmadi-Givi et al. 2004; Willison et al. 2013). The release of latent heating is particularly important for the cyclone growth. The warm conveyor belt (Browning and Roberts 1994; Harrold 1973), which is

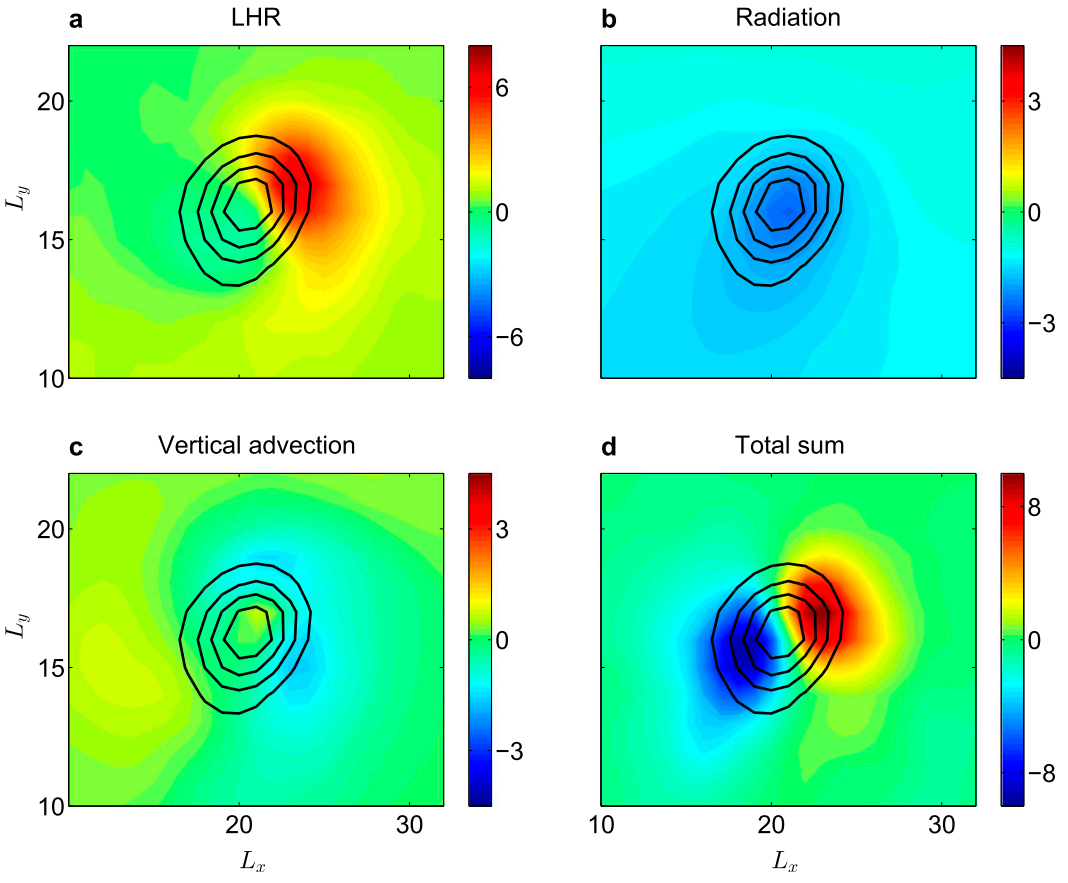

FIG. 10. The PV tendency from (a) diabatic heating due to LHR, (b) diabatic heating due to background radiation, (c) the vertical advection term, and (d) the sum of all the PV tendency terms. All quantities are normalized by 10^{-6} PVU s^{-1}. The black contours show the 780-hPa PV anomaly, with contours from 0.15 to 0.42 PVU and contour interval of 0.09 PVU. The longitudinal and latitudinal extents of the composite box are denoted by L_x and L_y, respectively.

associated with the motion of warm air that originates in the warm sector of the cyclone, travels parallel to the cold front and ascends upward in the vicinity of the warm front. As the warm and moist air travels upward and poleward, it cools and condenses, releasing latent heat. The resulting midtropospheric warming tends to produce a positive PV anomaly at low levels, slightly downstream of the warming (Stoelinga 1996), and a negative PV anomaly at upper levels (e.g., Ahmadi-Givi et al. 2004; Schemm and Wernli 2014; Methven 2015).

The contribution of diabatic heating associated with LHR can be calculated using Eq. (3), with the rate of latent heating $(d\theta/dt)_{\mathrm{LHR}}$ evaluated using the expression derived by Emanuel et al. (1987),

$$\left(\frac{d\theta}{dt}\right)_{\mathrm{LHR}} = \omega\left(\frac{\partial\theta}{\partial p} - \frac{\gamma_m}{\gamma_d}\frac{\theta}{\theta_E}\frac{\partial\theta_E}{\partial p}\right), \tag{5}$$

where θ_E is the equivalent potential temperature; γ_m and γ_d are the moist and dry lapse rates, respectively; and ω is the vertical velocity in pressure coordinates. For a dry atmosphere $\gamma_m = \gamma_d$, $\theta = \theta_E$, and, hence, by definition $(d\theta/dt)_{\mathrm{LHR}} = 0$.

Focusing on the vertical axis, the PV tendency due to LHR is then approximately given by

$$\frac{dq}{dt} = -g(f+\zeta)\frac{\partial}{\partial p}\left(\frac{d\theta}{dt}\right)_{\mathrm{LHR}}, \tag{6}$$

where ζ is the relative vorticity in the vertical direction.

The PV tendency associated with LHR from the cyclone composite (Fig. 10a), shows a large positive maximum on the northeastern side of the cyclone. Thus, LHR acts to propagate the low-level PV anomaly eastward and poleward. Note that the maximum PV tendency from LHR coincides with the location of strong positive vertical and poleward velocities (Fig. 4b and Fig. 4c, respectively), residing in a region of warm and moist air (Fig. 4d).

The latent heating in the midtroposphere acts, in general, to widen the isentropes at upper levels, above the warming, and to narrow them at lower levels, below the warming (see the schematic illustration in Fig. 11a). Thus, the static stability increases at lower levels (as $\partial\dot{\theta}/\partial p$ becomes larger in absolute value), and decreases at upper levels. In addition, the warming tends to increase the geopotential height at upper levels, and the resulting unbalanced outward pressure gradient force produces divergence at upper levels. This leads to upward vertical motion and convergence at lower levels that increases the relative vorticity there. Since the PV tendency is proportional to the product of the absolute vorticity and to the rate of change of static stability [Eq. (6)], the two processes, therefore, act to increase the low-level PV and deepen the low-level cyclone.

As a result of the inherent asymmetry of the cyclone, which advects high temperatures to its east and cold temperatures to its west, the mechanism described above occurs on the eastern side of the cyclone. Hence, LHR and its associated low-level PV tendency are maximized on the northeastern side of the cyclone, where warm and moist air ascends, cools, and condenses (as illustrated in the schematic Fig. 11b). This contributes to an eastward and poleward propagation of the low-level cyclone.

The propagation mechanism described above is reminiscent to that of diabatic Rossby vortices (DRVs) (Parker and Thorpe 1995; Moore and Montgomery 2005; Moore et al. 2008, 2013). DRVs can grow as a result of an approximate phase locking and mutual amplification of two diabatically generated PV anomalies: a low-level positive (cyclonic) PV anomaly and a midtropospheric negative (anticyclonic) PV anomaly. In the absence of an upper trough, these vortices can self-advect themselves through the diabatic generation of PV along the warm frontal zone.

The diabatic heating by LHR probably has an additional indirect effect on the poleward propagation of the low-level PV (Coronel et al. 2015). At upper levels, above the area of heating, the diabatic PV tendency is negative, thus acting to enhance the downstream ridge (anticyclone) in our simulation (not shown). As a result, an upper-level PV dipole is formed. This enhances the poleward advection of the low-level PV.

Next, we also present the PV tendency from diabatic heating associated with radiation, calculated using Eq. (2) with $(d\theta/dt)_{\text{rad}}$, which has a smaller negative contribution (Fig. 10b). Since radiation overall warms the surface of Earth, it tends to widen the isentropes above. Hence, at every level above the ground, the cyclone experiences a negative PV tendency. Note that the southwest–northeast structure observed originates from the elongation of the absolute vorticity in that direction.

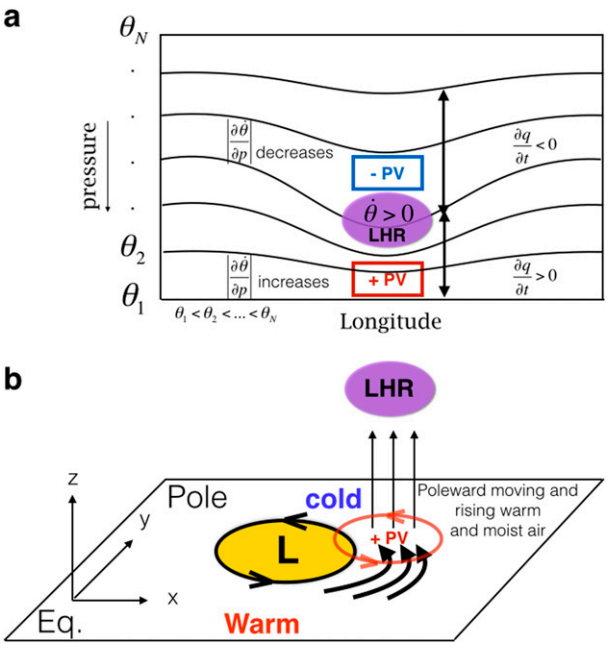

FIG. 11. (a) Schematic diagram illustrating the influence of LHR on the PV field. Midtropospheric warming associated with LHR increases (decreases) static stability at lower (upper) levels, thus producing a positive (negative) PV tendency there (denoted as +PV and −PV, respectively). (b) The schematic diagram illustrating the role of LHR in the poleward motion of the low-level cyclone. The yellow circle (L in the middle) with black circled arrows denotes the low-level cyclone and the direction of the velocity associated with it. The thick curved black arrows to its east represent the induced winds associated with the cyclone, and thin arrows represent upward motion. The warm and moist air to the south and east of the cyclone travels poleward and upward. As it cools, there is LHR (purple shading) in the midtroposphere, which acts to produce positive PV tendency at lower levels (light red circled arrows), which promotes an eastward and poleward motion of the low-level cyclone.

The vertical advection term (Fig. 10c) is found to be of even smaller magnitude, and acts in general to weaken (strengthen) the PV anomaly on its eastward (westward) side. This is a result of the structure of the background PV, which increases with height, and dominates the vertical gradient. Hence, the upward motion associated with the cyclone on its eastern side, and the much weaker downward vertical velocity to its east (Fig. 4b), advects low (high) PV to the east (west) of the low-level PV.

The sum of all the PV tendency terms (Fig. 10d), including the horizontal advection terms, gives an overall positive (negative) PV tendency on the northeastern (southwestern) side of the lower-level PV, and negative PV tendency elsewhere. Hence, when combined together, all the terms on the rhs of Eq. (4) act to propagate the PV anomaly toward the northeast direction. Comparing the total sum (Fig. 10d) with the actual PV

tendency from the low-level PV composite (Fig. 5), shows good agreement, although the structure slightly differ. This could be a result of friction, which is not taken into account in this balance. Although probably small at the levels chosen here, it is known in general to influence the PV at low levels (Stoelinga 1996). Nevertheless, the overall structure of the total PV tendency recovers well the positive PV tendency on the northeastern side of the low-level PV, consistent with the northeastward motion of the low-level cyclones.

Note that the PV tendency due to LHR is comparable but slightly larger than the PV tendency due to the horizontal advection terms (a maximum PV tendency of 7.06 and 6.22 PVU s^{-1}, respectively; 1 PVU = 10^{-6} K kg^{-1} m^2 s^{-1}). In fact, the diabatic heating rate as a result of LHR is possibly slightly underestimated in magnitude.[2] Hence, it appears that the PV tendency due to LHR is stronger than the PV tendency due to the advection terms, although both terms are important for the poleward motion of the low-level cyclone.

7. Time development of the cyclone composites

As a next step, we composite the cyclones at different stages of their evolutions, to examine whether the dominant mechanisms through which cyclones propagate poleward change over the course of their evolution.

The composites are centered on the time of peak intensity (denoted as τ_0), and then calculated every 6 h, from 1 day prior to the time of peak PV intensity, and up to 1 day afterward. Figure 12 shows selected PV composites at $\tau_0 - 24$ h, $\tau_0 - 12$ h, τ_0, and $\tau_0 + 24$ h (from left to right, respectively) of the total PV tendency (Fig. 12a), the PV tendency due to LHR (Fig. 12b), the PV tendency due to horizontal advection (Fig. 12c), and the time development of the low-level (color shaded contours) and upper-level (black contours) PV anomalies (Fig. 12d). In all panels of Figs. 12a–c, the low-level PV anomaly at that time is shown in black contours for reference.

The basic mechanism for poleward propagation is similar during the growth of the cyclone (cf. the three first columns in Fig. 12), while the composites differ greatly in the weakening phase of the cyclone, as expected (rightmost column in Fig. 12). The total PV tendency, the PV tendency due to LHR, and the PV tendency due to horizontal advection are all maximized at the time of peak intensity. This is consistent with the PV tendency terms being proportional to both the PV anomaly and the velocity field, which are strongest at the time of peak intensity. Note that the relative effect of these PV tendencies depends on how big the PV anomaly is at that time, and, therefore, the effective tendencies should be normalized. The normalized tendencies (not shown) reveal that, in fact, both the total PV tendency and the LHR are maximized 12 h prior to the cyclone peak intensity (at the time of maximal growth rate). All other features are, otherwise, similar.

The PV tendencies in Fig. 12 appear to produce a more meridionally tilted structure throughout the growth stage of the cyclone. During the time development, the PV tendency due to LHR (Fig. 12b) produces a positive PV tendency that is less east–west oriented, and more concentrated in the northeastern side of the low-level PV. This is a result of the location of the upward motion of the warm and moist air, which is being concentrated more in this region. The sum of the nonlinear advection terms (not shown), induces a stronger and more poleward-oriented tendency throughout the time development of the low-level PV. This results in the more tilted structure of the horizontal advection terms (Fig. 12c), as well as the overall PV tendency (Fig. 12a). Thus, poleward propagation increases up to the time of peak intensity.

The time development of the lower and upper-level PV anomalies (Fig. 12d) shows some interesting features regarding their relative positions. During the growth of the low-level cyclone (first three panels from left in Fig. 12d), the meridional phase difference between the upper-level PV anomaly (black contours) and lower-level PV anomaly (colored contours), remains roughly the same during the life cycle of the cyclone. This implies that the upper and lower PV anomalies propagate poleward essentially at the same speed. On the contrary, the zonal phase difference between them becomes smaller, since the upper-level PV propagates faster toward the east than the lower-level PV, hence, the westward tilt with height decreases. This is consistent with classical theories of cyclogenesis and cyclolysis (e.g., Bjerknes 1919; Bjerknes and Solberg 1921; Schultz and Mass 1993).

Indeed, 24 h after the peak intensity, the upper-level PV is almost entirely above the low-level PV (rightmost panel in Fig. 12d), revealing a more barotropic structure. At that time, the total PV tendency is mainly negative (rightmost panel in Fig. 12a), consistent with the decaying of the low-level PV. In addition, the role of the LHR changes significantly at the decay stage (rightmost panel in Fig. 12b), with mostly negative PV tendency in

[2] According to Willison et al. (2013), the storm tracks exhibit sensitivity to the model resolution used, since moist diabatic processes are better resolved in a higher resolution. This results in stronger LHR and, therefore, stronger cyclones and more intense storm tracks. The resolution used for the current study, therefore, potentially underestimates the magnitude of the PV tendency due to LHR.

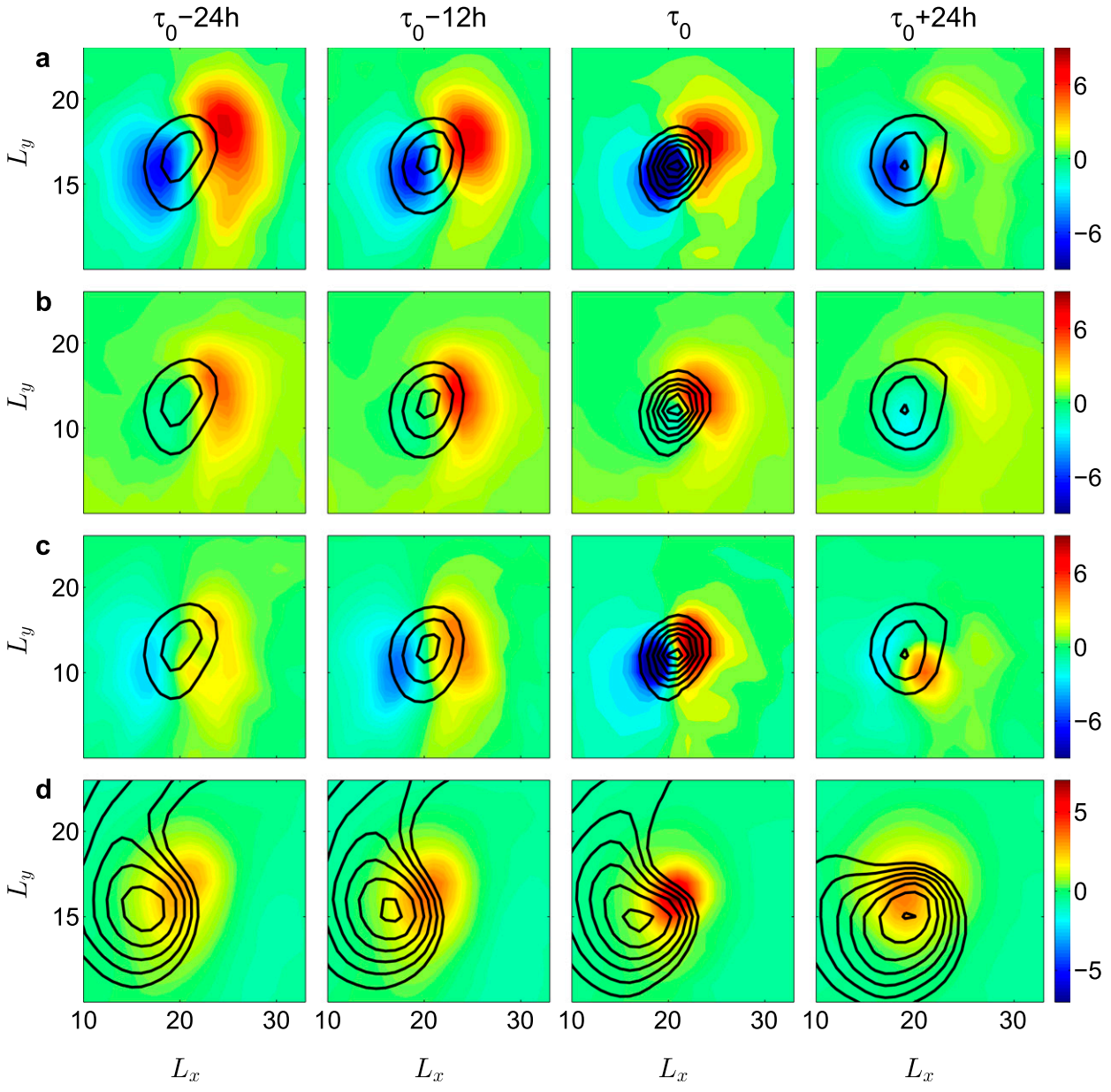

FIG. 12. Time development of PV composites. (a) The total PV tendency, (b) the PV tendency due to LHR, (c) the PV tendency due to horizontal advection, and (d) the low-level PV anomaly (colors) and upper-level PV anomaly (black contours), for composites at (left)–(right) $\tau_0 - 24$ h, $\tau_0 - 12$ h, τ_0, and $\tau_0 + 24$ h. In (a)–(c), quantities are normalized by 10^{-6} PVU s^{-1}. The low-level (780 hPa) PV anomaly at each time is shown in black contours for reference, with contour interval of 0.1 PVU and contour values ranging from 0.15 to 0.25, 0.35, 0.65, and 0.35 PVU for $\tau_0 - 24$ h, $\tau_0 - 12$ h, τ_0, and $\tau_0 + 24$ h, respectively. In (d), quantities are normalized by 10^{-7} PVU. The upper PV anomaly contour interval is 0.15 PVU, and contour values range from 0.45 to 1.05, 1.2, 1.2, and 1.3 PVU for $\tau_0 - 24$ h, $\tau_0 - 12$ h, τ_0, and $\tau_0 + 24$ h, respectively.

the cyclone core. This is associated with the intrusion of cold and dry air during the decay of the cyclone, which result in loss of access to warm and moist air and decrease in the upward vertical velocity.

The structure of the horizontal advection also changes significantly during the decay stage (rightmost panel in Fig. 12c), with a much weaker eastward advection, and no sign for any poleward deflection. In fact, the nonlinear advection terms at this stage (not shown) now act to advect the low-level PV westward and slightly equatorward, counterbalancing the weak eastward advection by the mean. This is a result of the position of the upper-level PV relative to the lower-level PV anomaly (rightmost panel in Fig. 12d).

Because there is no longer a westward tilt with height, there is no induced poleward velocity at low levels from the upper-level PV. Hence, the mechanism of poleward advection by the upper-level PV, that was demonstrated in section 5b using the piecewise PV inversion, is absent (or even reversed) during the decay of the low-level cyclone.

8. Dependence on cyclone intensity

Finally, we examine how the cyclone composites and the poleward propagation depend on the intensity of the cyclone. For this purpose, we partition the cyclones into categories, based on peak intensity, and perform separate composites for every group. To improve the statistics, a longer run of 2000 days (where nearly 4800 cyclones were identified) is used. The cyclones were divided into six groups from the weakest 800 cyclones (denoted as group 1) to the strongest 800 cyclones (denoted as group 6).

Figure 13 shows the low-level (colored contours) and upper-level (black contours) PV anomalies, for group 6 (Fig. 13a), group 5 (Fig. 13b), group 3 (Fig. 13c), and group 1 (Fig. 13d), corresponding to an averaged low-level maximum PV intensity of 0.58, 0.36, 0.2, and 0.07 PVU, respectively. The relative positions of the upper- and lower-level PV anomalies reveal that the vertical structure differs for cyclones of different intensities. While stronger cyclones have the characteristic baroclinic structure of a westward tilt with height (Figs. 13a,b), weaker cyclones exhibit a more barotropic structure, where the two PV anomalies are more vertically aligned (Figs. 13c,d).

This implies that the PV tendency due to LHR and the horizontal advection (and thus the overall PV tendency) are expected to be smaller for the weaker cyclones. Indeed, Fig. 14a shows that the maximum values of the normalized total PV tendency (red), the normalized PV due to horizontal advection (blue), and the normalized PV tendency due to LHR (green), all increase as the averaged maximum intensity of the composite group increases. Horizontal advection appears to be a more significant process for weaker intensities, while LHR becomes more important at higher intensities. Note that for comparison purposes, the normalized tendencies are shown (all PV tendency are normalized by the maximum PV anomaly of the corresponding composite group, to give the effective tendency). However, the results are essentially the same for the unnormalized tendencies.

The net poleward propagation of each intensity group (calculated as the latitudinal difference between the initial position and the position at the time of maximum

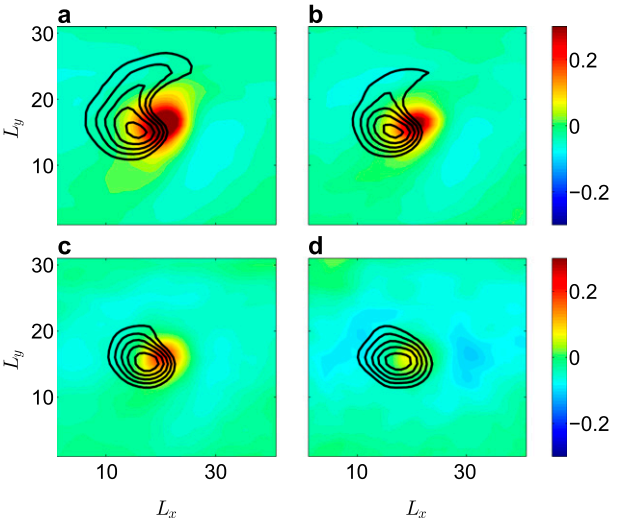

FIG. 13. (a) The low-level PV anomaly (colors) and upper-level PV anomaly (black contours) for (a) intensity group 6, (b) intensity group 5, (c) intensity group 3, and (d) intensity group 1, corresponding to an averaged low-level maximum PV intensity of 0.58, 0.36, 0.2, and 0.07 PVU, respectively. The upper-level PV contours range from 0.5 to 1.1 PVU, with contour interval of 0.15 PVU.

intensity averaged for all the cyclones in the composite group), also increases with intensity (Fig. 14b). This confirms our earlier conjecture that stronger cyclones also propagate more poleward. A more intense PV anomaly is also associated with stronger velocities; hence both horizontal advection and LHR are larger. In addition, the more barotropic structure of the weaker cyclones means that the nonlinear poleward advection by the upper-level PV is weaker, as discussed for the case of a decaying cyclone in the previous section. Hence, the larger poleward deflection and the higher tendencies associated with the stronger cyclones are consistent with our propagation mechanism.

9. Summary and discussion

The poleward motion of midlatitude cyclones and the corresponding downstream poleward tilt of localized storm tracks (Fig. 1) is studied here from a Lagrangian PV perspective. While the crucial role of transient eddies in the poleward deflection of the storm tracks is known in a statistical time-mean balance sense (e.g., Orlanski 1998), the equilibrium state cannot give a complete understanding of how such a balance is achieved. The current study highlights the basic mechanism for poleward tendency of storms from a single storm perspective.

A detailed PV budget, based on composites of extratropical cyclones in an idealized GCM, reveals the important role of the upper-level PV and the

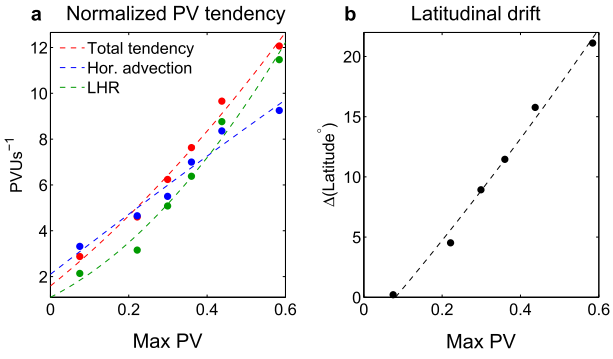

FIG. 14. The dependence on the averaged low-level maximum PV intensity of (a) the normalized total PV tendency (red), the normalized PV tendency due to horizontal advection (blue), and the normalized PV tendency due to LHR (green), and (b) the averaged latitudinal drift of the cyclones. Normalization is achieved by dividing the actual tendencies by the maximum intensity of the corresponding composite group. Dashed lines in each plot show the corresponding best-fit line.

diabatic heating associated with LHR in the poleward motion of the low-level cyclone. The interaction with the upper-level PV and the release of latent heating are both well-established processes in the context of cyclogenesis, and are known to have an important role in the growth of surface cyclones (e.g., Hoskins et al. 1985). Here, we emphasize that these processes are also important for the poleward tendency of the low-level cyclones.

In the PV framework, the cyclogenesis process is explained by the mutual amplification of the upper- and lower-level PV anomalies. This interaction is linear since it involves advection of the background PV by the perturbations at the other level. The cyclone's poleward motion, however, turns out to be related to the nonlinear advection terms (Fig. 6c).

A piecewise PV inversion technique is used to decompose the low-level nonlinear PV advection terms into contributions from upper, lower, and surface PV anomalies (the latter is associated with the surface temperature anomaly), and the contribution to the PV tendency resulting from each of the PV perturbations is analyzed separately (Fig. 8). The nonlinear poleward advection by the upper-level PV is found to be the dominant term in this decomposition, responsible for the overall poleward tendency in the nonlinear advection terms. The poleward motion of the low-level PV is thus a basic property of baroclinic instability (although it is crucially a nonlinear phenomenon, and therefore does not occur for linear baroclinic waves). The resulting westward tilt with height implies that the induced meridional velocity on the low-level cyclone, which is located to the east of the upper trough, is always poleward (Fig. 9). This can be considered a baroclinic analog to the barotropic beta effect (Gilet et al. 2009; Oruba et al. 2013), which is often used to explain the poleward motion of oceanic vortices and tropical cyclones (e.g., McWilliams and Flierl 1979; Wu and Emanuel 1993).

The same considerations could lead us to the conclusion that the positive upper PV anomaly should propagate equatorward. However, since the upper-level PV is much stronger than the lower-level PV, the nonlinear advection from the lower-level PV is weaker. This was verified by performing a piecewise PV inversion for the upper-level winds (not shown).

The PV analysis also emphasizes the crucial role of LHR in the poleward motion of the cyclone (Fig. 10). As a result of the inherent zonal asymmetry of the cyclone, whose winds transport poleward warm and moist tropical air to its east, LHR is maximized on its northeastern side. This, in general, increases both the static stability and the absolute vorticity at lower levels; hence, strengthening the PV perturbation at lower levels (Fig. 11). Thus, a strong positive PV tendency forms at lower levels, propagating the anomaly eastward and poleward.

The conclusions drawn here may potentially be used to explain the differences between cyclone and anticyclone propagation. High pressure systems, associated with anticyclonic motion, are usually located on the westward side of the upper-level trough. Thus, the induced upper-level winds tend to advect anticyclones equatorward. However, high pressure systems are characterized by downward motion (rather than upward as in cyclones). Hence, the additional effect caused by LHR that contributed to the poleward tendency of the low-level cyclones, does not occur for anticyclones. In addition, anticyclones are generally weaker than cyclones, hence, the PV tendencies associated with them are smaller. The equatorward tendency of anticyclones is, therefore, weaker, and is possibly reduced even further by the nonlinear interactions with neighboring cyclones.

Our study also showed that during the growth stage of the cyclone, the decomposition of the low-level PV tendency does not change much over time, although it changes significantly in the decaying stage. The poleward deflection appears to increase as the cyclone matures, but is completely halted by the end of the life cycle. This is consistent with the barotropization and vertical alignment that occurs as the cyclone decays. In addition, it was found that stronger cyclones tend to propagate more poleward (Fig. 14b). This is again related to the larger westward tilt with height that was found for stronger cyclones, compared to the more barotropic structure that characterizes the weaker ones.

Although the treatment in this study was zonally symmetric, the mechanism described here to explain the poleward tendency of extratropical cyclones may also explain the poleward tilt of localized storm tracks, such as those observed in the NH. The localized temperature gradients off the NH eastern continental boundaries result in regions of high baroclinicity; hence, more storms are being generated locally in these regions. Once formed, the cyclones potentially drift poleward in a similar manner to that described above. The higher baroclinicity often results in enhanced downstream EKE (e.g., Kaspi and Schneider 2011, 2013), hence, stronger storms that are also characterized by stronger PV anomalies and stronger velocities. Thus, both the nonlinear interaction and the LHR are larger. Therefore, we expect in general to find higher deflection of storms in localized storm tracks compared to the zonally symmetric case presented here.

These arguments may also help to understand the observed difference between the tilt of the Pacific and the Atlantic storm track. Since the latter is characterized by larger EKE (Deng and Mak 2006; Mak and Deng 2007, see also Fig. 1), which implies stronger cyclones, both the LHR and the poleward advection by the upper-level PV are expected to be larger. This can result in larger poleward deflection of storms in the Atlantic storm track compared to the Pacific, which is consistent with the more tilted storm track observed there (Fig. 1).

Acknowledgments. The authors thank Kevin Hodges for his generosity in providing his tracking algorithm, and his kind help with implementing it. We also thank Lodovicia Illari and Morgan O'Neill for their help with the PV inversion code, Eli Galanti for his assistance in implementing it with the GCM composites, and Nili Harnik for valuable discussions throughout this study. Finally, the authors wish to thank two anonymous reviewers, whose insightful comments and suggestions helped to improve the manuscript. This research has been supported by the Israeli Science Foundation (1310/12 and 1859/12), and a EU-FP7 Marie Curie Career Integration Grant (CIG-304202).

REFERENCES

Ahmadi-Givi, F., G. C. Graig, and R. S. Plant, 2004: The dynamics of a midlatitude cyclone with very strong latent-heat release. *Quart. J. Roy. Meteor. Soc.*, **130**, 295–323, doi:10.1256/qj.02.226.

Bauer, M., and A. D. Del Genio, 2006: Composite analysis of winter cyclones in a GCM: Influence on climatological humidity. *J. Climate*, **19**, 1652–1672, doi:10.1175/JCLI3690.1.

Bjerknes, J., 1919: On the structure of moving cyclones. *Mon. Wea. Rev.*, **47**, 95–99, doi:10.1175/1520-0493(1919)47<95:OTSOMC>2.0.CO;2.

——, and H. Solberg, 1921: Life cycle of cyclones and the polar front theory of atmospheric circulation. *Geofys. Publ.*, **3**, 3–18.

Black, R. X., and R. M. Dole, 1993: The dynamics of large-scale cyclogenesis over the North Pacific Ocean. *J. Atmos. Sci.*, **50**, 421–442, doi:10.1175/1520-0469(1993)050<0421:TDOLSC>2.0.CO;2.

Blackmon, M., J. Wallace, N. Lau, and S. Mullen, 1977: An observational study of the Northern Hemisphere wintertime circulation. *J. Atmos. Sci.*, **34**, 1040–1053, doi:10.1175/1520-0469(1977)034<1040:AOSOTN>2.0.CO;2.

Blender, R., K. Fraedrich, and F. Lunkeit, 1997: Identification of cyclone-track regimes in the North Atlantic. *Quart. J. Roy. Meteor. Soc.*, **123**, 727–741, doi:10.1002/qj.49712353910.

Brayshaw, D. J., B. Hoskins, and M. Blackburn, 2008: The storm-track response to idealized SST perturbations in an aquaplanet GCM. *J. Atmos. Sci.*, **65**, 2842–2860, doi:10.1175/2008JAS2657.1.

——, ——, and ——, 2009: The basic ingredients of the North Atlantic storm track. Part I: Land–sea contrast and orography. *J. Atmos. Sci.*, **66**, 2539–2558, doi:10.1175/2009JAS3078.1.

Brennan, M. J., G. M. Lackmann, and K. M. Mahoney, 2008: Potential vorticity (PV) thinking in operations: The utility of nonconservation. *Wea. Forecasting*, **23**, 168–182, doi:10.1175/2007WAF2006044.1.

Bretherton, F. P., 1966: Baroclinic instability and the short wavelength cut-off in terms of potential vorticity. *Quart. J. Roy. Meteor. Soc.*, **92**, 335–345, doi:10.1002/qj.49709239303.

Broccoli, A., and S. Manabe, 1992: The effects of orography on midlatitude Northern Hemisphere dry climates. *J. Climate*, **5**, 1181–1201, doi:10.1175/1520-0442(1992)005<1181:TEOOOM>2.0.CO;2.

Browning, K. A., and N. M. Roberts, 1994: Structure of a frontal cyclone. *Quart. J. Roy. Meteor. Soc.*, **120**, 1535–1557, doi:10.1002/qj.49712052006.

Cai, M., S. Yang, H. M. Van den Dool, and V. E. Kousky, 2007: Dynamical implications of the orientation of atmospheric eddies: A local energetics perspective. *Tellus*, **59A**, 127–140, doi:10.1111/j.1600-0870.2006.00213.x.

Catto, J. L., L. C. Shaffrey, and K. I. Hodges, 2010: Can climate models capture the structure of extratropical cyclones? *J. Climate*, **23**, 1621–1635, doi:10.1175/2009JCLI3318.1.

Chang, E. K. M., S. Lee, and K. L. Swanson, 2002: Storm track dynamics. *J. Climate*, **15**, 2163–2183, doi:10.1175/1520-0442(2002)015<02163:STD>2.0.CO;2.

Charney, J., 1947: The dynamics of long waves in a baroclinic westerly current. *J. Meteor.*, **4**, 136–162, doi:10.1175/1520-0469(1947)004<0136:TDOLWI>2.0.CO;2.

——, 1955: The use of the primitive equations of motion in numerical prediction. *Tellus*, **7A**, 22–26, doi:10.1111/j.2153-3490.1955.tb01138.x.

Coronel, B., D. Ricard, G. Rivière, and P. Arbogast, 2015: Role of moist processes in the tracks of idealized midlatitude surface cyclones. *J. Atmos. Sci.*, **72**, 2979–2996, doi:10.1175/JAS-D-14-0337.1.

Davies, H. C., and C. H. Bishop, 1994: Eady edge waves and rapid development. *J. Atmos. Sci.*, **51**, 1930–1946, doi:10.1175/1520-0469(1994)051<1930:EEWARD>2.0.CO;2.

Davis, C. A., 1992: Piecewise potential vorticity inversion. *J. Atmos. Sci.*, **49**, 1397–1411, doi:10.1175/1520-0469(1992)049<1397:PPVI>2.0.CO;2.

——, and K. A. Emanuel, 1991: Potential vorticity diagnostics of cyclogenesis. *Mon. Wea. Rev.*, **119**, 1929–1953, doi:10.1175/1520-0493(1991)119<1929:PVDOC>2.0.CO;2.

——, M. T. Stoelinga, and Y.-H. Kuo, 1993: The integrated effect of condensation in numerical simulations of extratropical

cyclogenesis. *Mon. Wea. Rev.*, **121**, 2309–2330, doi:10.1175/1520-0493(1993)121<2309:TIEOCI>2.0.CO;2.

Deng, Y., and M. Mak, 2006: Nature of the differences in the intraseasonal variability of the Pacific and Atlantic storm tracks: A diagnostic study. *J. Atmos. Sci.*, **63**, 2602–2615, doi:10.1175/JAS3749.1.

Eady, E., 1949: Long waves and cyclone waves. *Tellus*, **1A**, 33–52, doi:10.1111/j.2153-3490.1949.tb01265.x.

Emanuel, K., M. Fantini, and A. Thorpe, 1987: Baroclinic instability in an environment of small stability to slantwise moist convection. Part I: Two-dimensional models. *J. Atmos. Sci.*, **44**, 1559–1573, doi:10.1175/1520-0469(1987)044<1559:BIIAEO>2.0.CO;2.

Feldstein, S. B., 1998: An observational study of the intraseasonal poleward propagation of zonal mean flow anomalies. *J. Atmos. Sci.*, **55**, 2516–2529, doi:10.1175/1520-0469(1998)055<2516:AOSOTI>2.0.CO;2.

Frierson, D., I. Held, and P. Zurita-Gotor, 2006: A gray-radiation aquaplanet moist GCM. Part I: Static stability and eddy scale. *J. Atmos. Sci.*, **63**, 2548–2566, doi:10.1175/JAS3753.1.

Gilet, J., M. Plu, and G. Rivière, 2009: Nonlinear baroclinic dynamics of surface cyclones crossing a zonal jet. *J. Atmos. Sci.*, **66**, 3021–3041, doi:10.1175/2009JAS3086.1.

Hakim, G. J., D. Keyser, and L. F. Bosart, 1996: The Ohio Valley wave-merger cyclogenesis event of 25–26 January 1978. Part II: Diagnosis using quasigeostrophic potential vorticity inversion. *Mon. Wea. Rev.*, **124**, 2176–2205, doi:10.1175/1520-0493(1996)124<2176:TOVWMC>2.0.CO;2.

Harrold, T. W., 1973: Mechanisms influencing the distribution of precipitation within baroclinic disturbances. *Quart. J. Roy. Meteor. Soc.*, **99**, 232–251, doi:10.1002/qj.49709942003.

Held, I. M., 1982: On the height of the tropopause and the static stability of the troposphere. *J. Atmos. Sci.*, **39**, 412–417, doi:10.1175/1520-0469(1982)039<0412:OTHOTT>2.0.CO;2.

——, 1983: Stationary and quasi-stationary eddies in the extratropical troposphere: Theory. *Large-Scale Dynamical Processes in the Atmosphere*, B. Hoskins, and R. Pearce, Eds., Academic Press, 127–168.

——, and M. Ting, 1990: Orographic versus thermal forcing of stationary waves: The importance of the mean low-level wind. *J. Atmos. Sci.*, **47**, 495–500, doi:10.1175/1520-0469(1990)047<0495:OVTFOS>2.0.CO;2.

Hodges, K. I., 1995: Feature tracking on the unit sphere. *Mon. Wea. Rev.*, **123**, 3458–3465, doi:10.1175/1520-0493(1995)123<3458:FTOTUS>2.0.CO;2.

——, 1999: Adaptive constraints for feature tracking. *Mon. Wea. Rev.*, **127**, 1362–1373, doi:10.1175/1520-0493(1999)127<1362:ACFFT>2.0.CO;2.

——, B. J. Hoskins, J. Boyle, and C. Thorncroft, 2003: A comparison of recent reanalysis datasets using objective feature tracking: Storm tracks and tropical easterly waves. *Mon. Wea. Rev.*, **131**, 2012–2037, doi:10.1175/1520-0493(2003)131<2012:ACORRD>2.0.CO;2.

Holland, G. J., 1983: Tropical cyclone motion: Environmental interaction plus a beta effect. *J. Atmos. Sci.*, **40**, 328–342, doi:10.1175/1520-0469(1983)040<0328:TCMEIP>2.0.CO;2.

Hoskins, B. J., and D. J. Karoly, 1981: The steady linear response of a spherical atmosphere to thermal and orographic forcing. *J. Atmos. Sci.*, **38**, 1179–1196, doi:10.1175/1520-0469(1981)038<1179:TSLROA>2.0.CO;2.

——, and P. Valdes, 1990: On the existence of storm tracks. *J. Atmos. Sci.*, **47**, 1854–1864, doi:10.1175/1520-0469(1990)047<1854:OTEOST>2.0.CO;2.

——, and K. Hodges, 2002: New perspectives on the Northern Hemisphere winter storm tracks. *J. Atmos. Sci.*, **59**, 1041–1061, doi:10.1175/1520-0469(2002)059<1041:NPOTNH>2.0.CO;2.

——, and ——, 2005: A new perspective on the Southern Hemisphere storm tracks. *J. Climate*, **18**, 4108–4129, doi:10.1175/JCLI3570.1.

——, I. James, and G. White, 1983: The shape, propagation, and mean–flow interaction of large-scale weather systems. *J. Atmos. Sci.*, **40**, 1595–1612, doi:10.1175/1520-0469(1983)040<1595:TSPAMF>2.0.CO;2.

——, M. E. McIntyre, and A. W. Robertson, 1985: On the use and significance of isentropic potential vorticity maps. *Quart. J. Roy. Meteor. Soc.*, **111**, 877–946, doi:10.1002/qj.49711147002.

Huo, Z., D. Zhang, and J. R. Gyakum, 1999a: Interaction of potential vorticity anomalies in extratropical cyclogenesis. Part I: Static piecewise inversion. *Mon. Wea. Rev.*, **127**, 2546–2562, doi:10.1175/1520-0493(1999)127<2546:IOPVAI>2.0.CO;2.

——, ——, and ——, 1999b: Interaction of potential vorticity anomalies in extratropical cyclogenesis. Part II: Sensitivity to initial perturbations. *Mon. Wea. Rev.*, **127**, 2563–2575, doi:10.1175/1520-0493(1999)127<2563:IOPVAI>2.0.CO;2.

Inatsu, M., H. Mukougawa, and S.-P. Xie, 2002: Stationary eddy response to surface boundary forcing: Idealized GCM experiments. *J. Atmos. Sci.*, **59**, 1898–1915, doi:10.1175/1520-0469(2002)059<1898:SERTSB>2.0.CO;2.

James, P. M., K. Fraedrich, and I. N. James, 1994: Wave-zonal-flow interaction and ultra-low-frequency variability in a simplified global circulation model. *Quart. J. Roy. Meteor. Soc.*, **120**, 1045–1067, doi:10.1002/qj.49712051812.

Kaspi, Y., and T. Schneider, 2011: Downstream self-destruction of storm tracks. *J. Atmos. Sci.*, **68**, 2459–2464, doi:10.1175/JAS-D-10-05002.1.

——, and ——, 2013: The role of stationary eddies in shaping midlatitude storm tracks. *J. Atmos. Sci.*, **70**, 2596–2613, doi:10.1175/JAS-D-12-082.1.

Kieu, C. Q., and D. Zhang, 2010: A piecewise potential vorticity inversion algorithm and its application to hurricane inner-core anomalies. *J. Atmos. Sci.*, **67**, 2616–2631, doi:10.1175/2010JAS3421.1.

Klein, W., 1957: Principal tracks and mean frequencies of cyclones and anticyclones in the Northern Hemisphere. U.S. Weather Bureau, 60 pp.

Lackmann, G. M., 2002: Cold-frontal potential vorticity maxima, the low-level jet, and moisture transport in extratropical cyclones. *Mon. Wea. Rev.*, **130**, 59–74, doi:10.1175/1520-0493(2002)130<0059:CFPVMT>2.0.CO;2.

Lee, S., S. Son, K. Grise, and S. B. Feldstein, 2007: A mechanism for the poleward propagation of zonal mean flow anomalies. *J. Atmos. Sci.*, **64**, 849–868, doi:10.1175/JAS3861.1.

Macdonald, N. J., 1967: The dependence of the motion of cyclonic and anticyclonic vortices on their size. *J. Atmos. Sci.*, **24**, 449–452, doi:10.1175/1520-0469(1967)024<0449:TDOTMO>2.0.CO;2.

Mak, M., and Y. Deng, 2007: Diagnostic and dynamical analyses of two outstanding aspects of storm tracks. *Dyn. Atmos. Oceans*, **43**, 80–99, doi:10.1016/j.dynatmoce.2006.06.004.

Marciano, C. G., G. M. Lackmann, and W. A. Robinson, 2015: Changes in U.S. East Coast cyclone dynamics with climate change. *J. Climate*, **28**, 468–484, doi:10.1175/JCLI-D-14-00418.1.

Martin, J. E., 2006: *Mid-Latitude Atmospheric Dynamics: A First Course.* Wiley, 336 pp.

McWilliams, J. C., and G. R. Flierl, 1979: On the evolution of isolated, nonlinear vortices. *J. Phys. Oceanogr.*, **9**, 1155–1182, doi:10.1175/1520-0485(1979)009<1155:OTEOIN>2.0.CO;2.

Mendes, D., and M. D. Mendes, 2004: Climatology of cyclones, anticyclones and storm tracks: Revision of concepts. *Rev. Bras. Geofís.*, **22**, 127–134, doi:10.1590/S0102-261X2004000200003.

Methven, J., 2015: Potential vorticity in warm conveyor belt outflow. *Quart. J. Roy. Meteor. Soc.*, **141**, 1065–1071, doi:10.1002/qj.2393.

Moore, R. W., and M. T. Montgomery, 2005: Analysis of an idealized, three-dimensional diabatic Rossby vortex: A coherent structure of the moist baroclinic atmosphere. *J. Atmos. Sci.*, **62**, 2703–2725, doi:10.1175/JAS3472.1.

——, ——, and H. C. Davies, 2008: The integral role of a diabatic Rossby vortex in a heavy snowfall event. *Mon. Wea. Rev.*, **136**, 1878–1897, doi:10.1175/2007MWR2257.1.

——, ——, and H. Davies, 2013: Genesis criteria for diabatic Rossby vortices: A model study. *Mon. Wea. Rev.*, **141**, 252–263, doi:10.1175/MWR-D-12-00080.1.

Nakamura, H., and A. Shimpo, 2004: Seasonal variations in the Southern Hemisphere storm tracks and jet streams as revealed in a reanalysis dataset. *J. Climate*, **17**, 1828–1844, doi:10.1175/1520-0442(2004)017<1828:SVITSH>2.0.CO;2.

Novak, L., M. H. P. Ambaum, and R. Tailleux, 2015: The life cycle of the North Atlantic storm track. *J. Atmos. Sci.*, **72**, 821–833, doi:10.1175/JAS-D-14-0082.1.

Orlanski, I., 1998: Poleward deflection of storm tracks. *J. Atmos. Sci.*, **55**, 2577–2602, doi:10.1175/1520-0469(1998)055<2577:PDOST>2.0.CO;2.

Oruba, L., G. Lapeyre, and G. Rivière, 2012: On the northward motion of midlatitude cyclones in a barotropic meandering jet. *J. Atmos. Sci.*, **69**, 1793–1810, doi:10.1175/JAS-D-11-0267.1.

——, ——, and ——, 2013: On the poleward motion of midlatitude cyclones in a baroclinic meandering jet. *J. Atmos. Sci.*, **70**, 2629–2649, doi:10.1175/JAS-D-12-0341.1.

Palmen, E., and C. W. Newton, 1969: *Atmospheric Circulation Systems: Their Structural and Physical Interpretation*. International Geophysics Series, Vol. 13, Academic Press, 602 pp.

Parker, D. J., and A. J. Thorpe, 1995: Conditional convective heating in a baroclinic atmosphere: A model of convective frontogenesis. *J. Atmos. Sci.*, **52**, 1699–1711, doi:10.1175/1520-0469(1995)052<1699:CCHIAB>2.0.CO;2.

Peixoto, J. P., and A. H. Oort, 1992: *Physics of Climate*. American Institute of Physics, 520 pp.

Petterssen, S., 1956: *Motion and Motion Systems*. Vol. 2, *Weather Analysis and Forecasting*, McGraw-Hill, 428 pp.

Pfahl, S., P. A. O'Gorman, and M. S. Singh, 2015: Extratropical cyclones in idealized simulations of changed climates. *J. Climate*, **28**, 9373–9392, doi:10.1175/JCLI-D-14-00816.1.

Plant, R. S., G. C. Craig, and S. L. Gray, 2003: On a threefold classification of extratropical cyclogenesis. *Quart. J. Roy. Meteor. Soc.*, **129**, 2989–3012, doi:10.1256/qj.02.174.

Posselt, D. J., and J. E. Martin, 2004: The effect of latent heat release on the evolution of a warm occluded thermal structure. *Mon. Wea. Rev.*, **132**, 578–599, doi:10.1175/1520-0493(2004)132<0578:TEOLHR>2.0.CO;2.

Reed, R. J., M. T. Stoelinga, and Y.-H. Kuo, 1992: A model-aided study of the origin and evolution of the anomalously high potential vorticity in the inner region of a rapidly deepening marine cyclone. *Mon. Wea. Rev.*, **120**, 893–913, doi:10.1175/1520-0493(1992)120<0893:AMASOT>2.0.CO;2.

Riehl, H., T. C. Yeh, and N. E. La Seur, 1950: A study of variations of the general circulation. *J. Meteor.*, **7**, 181–194, doi:10.1175/1520-0469(1950)007<0181:ASOVOT>2.0.CO;2.

Rivière, G., 2009: Effect of latitudinal variations in low-level baroclinicity on eddy life cycles and upper-tropospheric wave-breaking processes. *J. Atmos. Sci.*, **66**, 1569–1592, doi:10.1175/2008JAS2919.1.

——, P. Arbogast, G. Lapeyre, and K. Maynard, 2012: A potential vorticity perspective on the motion of a mid-latitude winter storm. *Geophys. Res. Lett.*, **39**, L12808, doi:10.1029/2012GL052440.

Robinson, W. A., 2000: A baroclinic mechanism for the eddy feedback on the zonal index. *J. Atmos. Sci.*, **57**, 415–422, doi:10.1175/1520-0469(2000)057<0415:ABMFTE>2.0.CO;2.

Rossby, C., 1948: On displacements and intensity changes of atmospheric vortices. *J. Mar. Res.*, **7**, 175–187.

Rosting, B., and J. E. Kristjansson, 2012: The usefulness of piecewise potential vorticity inversion. *J. Atmos. Sci.*, **69**, 934–941, doi:10.1175/JAS-D-11-0115.1.

Sardeshmukh, P. D., and B. I. Hoskins, 1984: Spatial smoothing on the sphere. *Mon. Wea. Rev.*, **112**, 2524–2529, doi:10.1175/1520-0493(1984)112<2524:SSOTS>2.0.CO;2.

Schär, C., and H. Wernli, 1993: Structure and evolution of an isolated semi-geostrophic cyclone. *Quart. J. Roy. Meteor. Soc.*, **119**, 57–90, doi:10.1002/qj.49711950904.

Schemm, S., and H. Wernli, 2014: The linkage between the warm and the cold conveyor belts in an idealized extratropical cyclone. *J. Atmos. Sci.*, **71**, 1443–1459, doi:10.1175/JAS-D-13-0177.1.

Schultz, D. M., and C. F. Mass, 1993: The occlusion process in a midlatitude cyclone over land. *Mon. Wea. Rev.*, **121**, 918–940, doi:10.1175/1520-0493(1993)121<0918:TOPIAM>2.0.CO;2.

Simmons, A., and B. Hoskins, 1978: The life cycles of some nonlinear baroclinic waves. *J. Atmos. Sci.*, **35**, 414–432, doi:10.1175/1520-0469(1978)035<0414:TLCOSN>2.0.CO;2.

Sinclair, M. R., 1994: An objective cyclone climatology for the Southern Hemisphere. *Mon. Wea. Rev.*, **122**, 2239–2256, doi:10.1175/1520-0493(1994)122<2239:AOCCFT>2.0.CO;2.

——, 1997: Objective identification of cyclones and their circulation intensity, and climatology. *Wea. Forecasting*, **12**, 595–612, doi:10.1175/1520-0434(1997)012<0595:OIOCAT>2.0.CO;2.

Stoelinga, M. T., 1996: A potential vorticity-based study of the role of diabatic heating and friction in a numerically simulated baroclinic cyclone. *Mon. Wea. Rev.*, **124**, 849–874, doi:10.1175/1520-0493(1996)124<0849:APVBSO>2.0.CO;2.

Storari, H. T., and N. J. MacDonald, 1973: Relation between the average motion of cyclones and anticyclones and their shape. *J. Geophys. Res.*, **78**, 2685–2690, doi:10.1029/JC078i015p02685.

Trenberth, K. E., 1986: An assessment of the impact of transient eddies on the zonal flow during a blocking episode using localized Eliassen–Palm flux diagnostics. *J. Atmos. Sci.*, **43**, 2070–2087, doi:10.1175/1520-0469(1986)043<2070:AAOTIO>2.0.CO;2.

——, 1991: Storm tracks in the Southern Hemisphere. *J. Atmos. Sci.*, **48**, 2159–2178, doi:10.1175/1520-0469(1991)048<2159:STITSH>2.0.CO;2.

Vallis, G. K., 2006: *Atmospheric and Oceanic Fluid Dynamics*. Cambridge University Press, 745 pp.

Wallace, J. M., G.-H. Lim, and M. L. Blackmon, 1988: Relationship between cyclone tracks, anticyclone tracks and baroclinic waveguides. *J. Atmos. Sci.*, **45**, 439–462, doi:10.1175/1520-0469(1988)045<0439:RBCTAT>2.0.CO;2.

Wang, X., and D.-L. Zhang, 2003: Potential vorticity diagnosis of a simulated hurricane. Part I: Formulation and quasi-balanced flow. *J. Atmos. Sci.*, **60**, 1593–1607, doi:10.1175/2999.1.

Wang, Y., and G. J. Holland, 1996a: The beta drift of baroclinic vortices. Part I: Adiabatic vortices. *J. Atmos.*

Sci., **53**, 411–427, doi:10.1175/1520-0469(1996)053<0411:TBDOBV>2.0.CO;2.

——, and ——, 1996b: The beta drift of baroclinic vortices. Part II: Diabatic vortices. *J. Atmos. Sci.*, **53**, 3737–3756, doi:10.1175/1520-0469(1996)053<3737:TBDOBV>2.0.CO;2.

Wernli, H., S. Dirren, M. A. Liniger, and M. Zillig, 2002: Dynamical aspects of the life cycle of the winter storm 'Lothar' (24–26 December 1999). *Quart. J. Roy. Meteor. Soc.*, **128**, 405–429, doi:10.1256/003590002321042036.

Willison, J., W. A. Robinson, and G. M. Lackmann, 2013: The importance of resolving mesoscale latent heating in the North Atlantic storm track. *J. Atmos. Sci.*, **70**, 2234–2250, doi:10.1175/JAS-D-12-0226.1.

Wu, C., and K. A. Emanuel, 1993: Interaction of a baroclinic vortex with background shear: Application to hurricane movement. *J. Atmos. Sci.*, **50**, 62–76, doi:10.1175/1520-0469(1993)050<0062:IOABVW>2.0.CO;2.

——, and ——, 1995: Potential vorticity diagnostics of hurricane movement. Part I: A case study of Hurricane Bob (1991). *Mon. Wea. Rev.*, **123**, 69–92, doi:10.1175/1520-0493(1995)123<0069:PVDOHM>2.0.CO;2.

Zishka, K. M., and P. J. Smith, 1980: The climatology of cyclones and anticyclones over North America and surrounding ocean environs for January and July, 1950–77. *Mon. Wea. Rev.*, **108**, 387–401, doi:10.1175/1520-0493(1980)108<0387:TCOCAA>2.0.CO;2.